Nanoscale

PAPER

Check for updates

Polymeric-protein-MOF nanoparticles with stimuli-responsive disassembly and highly reproducible synthesis

Justin Van Houten,[a,b] Sarah E. S. Quail,[a,b] Melissa C. D'Amaral,[a,b] Kezia E. Suryoraharjo, [ID] [a,b] Abigail Richards,[a,b] Ruben Castillo Barberi,[a,b] Rachel Leigh Mander [ID] [a,b] and Alana F. Ogata [ID] *[a,b]

Metal–organic frameworks (MOFs), such as zeolitic imidazolate framework-8 (ZIF-8), offer a promising platform for therapeutic protein delivery due to their biocompatibility and tunable degradation properties. However, the clinical translation of protein-loaded MOFs has been limited by poor colloidal stability and a lack of robust, stimulus-responsive release mechanisms. Here, we present a proof-of-concept colloidally stable nanoparticle system composed of poly(acrylic acid) (PAA), bovine serum albumin (BSA), ZIF-8 and copper (Cu) or iron (Fe) ions, PAA@Cu/FeBSA@c-ZIF-8, designed for H_2O_2-responsive, multimodal therapeutic delivery. Through iterative design, we stabilised protein-loaded ZIF-8 nanoparticles with PAA and doped the system with Cu or Fe to enable Fenton-based H_2O_2 sensitivity. Upon exposure to biologically relevant H_2O_2 concentrations (40–100 μM), PAA@CuBSA@c-ZIF-8 and PAA@FeBSA@c-ZIF-8 nanoparticles release encapsulated BSA and the doped transition metal ions, demonstrating potential for protein therapy in tandem with reactive oxygen species (ROS)-mediated cytotoxicity. The PAA@BSA@c-ZIF-8, PAA@CuBSA@c-ZIF-8 and PAA@FeBSA@c-ZIF-8 exhibit consistent physiochemical properties across independent operators and scales, including particle size, ζ potential, and cargo release, as well as cytotoxicity. Importantly, we identify ROS production, measured by 2′,7′-dichlorodihydrofluorescein diacetate response, as a key critical quality attribute correlating with therapeutic potency. This work establishes a reproducible, H_2O_2-responsive nanoplatform towards application in cancer therapy and supports the broader use of quality attribute metrics in nanoparticle development.

Introduction

The development of stimuli-responsive metal organic frameworks (MOFs) opened new avenues for targeted drug delivery, with particular interest in systems that respond to elevated levels of hydrogen peroxide (H_2O_2) in disease microenvironments. H_2O_2 is present at increased concentrations in tumours and inflamed tissues, offering a selective chemical trigger for controlled therapeutic release.[1–4] Jia *et al.* developed poly(methyl methacrylate)-Fe-benzene tricarboxylate-polydopamine MOFs that responded to H_2O_2 and glutathione, enabling dopamine and Fe ion release.[5] Ma *et al.* used Matériaux de l'Institut Lavoisier (MIL)-101(Fe) MOFs functionalized with triethylenediamine-DNA fragments for peroxide-triggered photodynamic therapy.[6] Yu *et al.* designed MIL-100(Fe) systems co-

loaded with ceria nanoparticles and siRNA-retinoic acid conjugates to induce neurogenesis *via* peroxide-induced degradation.[7] Jin *et al.* achieved peroxide-activated carbon monoxide release using $MnBr(CO)_5$-loaded Ti-MOFs.[8] However, the applicability of these MOF systems are limited as their synthetic approaches rely on harsh reaction conditions incompatible with proteins that could serve as deliverable therapeutics.[5–8]

In contrast, zeolitic imidazolate framework-8 (ZIF-8) is a well-studied MOF that supports protein loading due to its aqueous, mild self-assembly synthetic conditions. ZIF-8 has also been used for the release of small molecules such as doxorubicin,[9] camptothecin,[10] 3-methyladenine,[11] 6-mercaptopurine,[12,13] carboplatin,[14] and 5-fluorouracil.[12] Typically, these drugs are taken up into the porous ZIF-8 and released under acidic conditions.[12] The release of protein from ZIF-8 has also been demonstrated for lactoferrin,[15] RNase A,[16] Cytochrome *c*[17] and liposomes.[18,19] In contrast to small molecules, large biomolecule loading occurs within the lattice of ZIF-8 *via in situ* encapsulation and pH-triggered structural disassembly is required for release.[20,21] However, pH-triggered degradation presents limitations. While tumour tissues exhibit

[a]Department of Chemical and Physical Sciences, University of Toronto Mississauga, 1867 Inner Circle Road, Mississauga, ON L5L 1C6, Canada.
E-mail: alana.ogata@utoronto.ca
[b]Chemistry, University of Toronto, 80 St. George Street, Toronto, ON M5S 3H6, Canada

low pH due to the Warburg effect,[22] acidic environments also occur naturally in healthy tissues such as the gastrointestinal tract and bladder,[23] which increases the risk of premature or off-target release and limits therapeutic precision. Furthermore, pH gradients are diffuse and variable, complicating spatial control of drug release.[2,23,24]

To enable peroxidase-like activity, studies have incorporated redox-active metal ions such as copper (Cu) or iron (Fe) into ZIF-8 frameworks to enable Fenton-like reactivity.[25–30] These doped ZIF-8 systems catalyse the generation of hydroxyl radicals ($^{\bullet}OH$) through interactions with H_2O_2, a process that has been studied and leveraged for cytotoxicity enhancement in cancer therapy.[27,28,30] Although these systems clearly demonstrate oxidative activity and radical-mediated biological effects, direct evidence of ZIF-8 H_2O_2-triggered protein release remains elusive.[27–30] However, we hypothesize that local nanoparticle damage derived from generated ROS will allow for protein release from protein@ZIF-8 nanoparticles.[31]

Here, we incorporate Fenton-active transition metal ions (Cu and Fe) into protein@colloidal-ZIF-8 nanoparticles through iterative design to achieve H_2O_2-responsive degradation. We leveraged Fenton chemistry by doping colloidally stable poly(acrylic acid)@bovine serum albumin@colloidal-ZIF-8 (PAA@BSA@c-ZIF-8) nanoparticles with Cu (PAA@CuBSA@c-ZIF8) and Fe (PAA@FeBSA@c-ZIF-8). Both metals facilitate Fenton-like reactions, catalysing the decomposition of H_2O_2 into reactive hydroxyl radicals ($\cdot OH$).[32,33] We validated the structural and colloidal reproducibility of PAA@CuBSA@c-ZIF-8, PAA@FeBSA@c-ZIF-8, and PAA@BSA@c-ZIF-8 through dynamic light scattering (DLS), ζ potential, nanoparticle tracking analysis (NTA), and scanning electron microscopy (SEM). We further confirmed the crystallinity and cationic composition of the nanoparticles via X-ray diffraction (XRD) and X-ray photoelectron spectroscopy (XPS). Protein release in response to H_2O_2 was monitored using the Bradford assay and DLS. The released BSA protein was characterized using size exclusion chromatography and circular dichroism. We assessed therapeutic potential by monitoring cytotoxicity in HeLa cells, where H_2O_2-mediated release of protein and ions from PAA@CuBSA@c-ZIF-8 and PAA@FeBSA@c-ZIF-8 induced dose-dependent cell death. Lastly, we demonstrate the reproducibility and scalability of the synthesis across two batch sizes and four independent operators. Critical quality attributes, including particle size, ζ potential, ion and protein release profiles, and half maximal inhibitory concentration (IC_{50}) values, were reproducible with coefficients of variation (COVs) below 20% demonstrating the platform's potential for clinical translation.

Materials

MilliQ water (<18.2 Ω). Zinc acetate dihydrate (99%), 2-methylimidazole (99%), $CuCl_2 \cdot 2(H_2O)$ (99%), $FeCl_3 \cdot 6(H_2O)$ (97%) and poly-acrylic acid (25–45 k M_n and <2000 M_n, 99%) were purchased from Sigma-Aldrich and used without further purification. Bovine serum albumin (BSA, lyophilized powder) was purchased from Sigma-Aldrich. HCl (conc., ACS Plus grade) and NaOH (10 N, 99%) were used for pH adjustments. Bradford assay reagents (#5000006) were purchased from BioShop. Hydrogen peroxide (H_2O_2, 30%) was purchased from Thermo Fisher. For ICP-AES analysis TraceCERT® standards (1000 ppm) were purchased from Sigma-Aldrich. For inductively coupled plasma-atomic emission spectroscopy analysis trace metal basis HNO_3 (67–70%, Sigma-Aldrich) was used. 3,3′,5,5′-Tetramethylbenzidine (TMB, >99%) was purchased from Sigma-Aldrich. Na_3PO_4 and NaCl were purchased from BioShop. 15% polyacrylamide gel, SDS loading dye and TRIS-glycine-SDS running buffer, pH 8.3 was made from reagents purchased from BioShop. The Mini-PROTEAN Tetra handcast system and electrophoresis chamber was used for SDS-PAGE experiments. SeeBlue™ Plus2 Protein Ladder from ThermoFisher (# LC5925) was used.

Cell work: for all cell work, aseptic technique was maintained throughout, and all cell experiments were performed within 5 cell passages. MilliQ water (<18.2 Ω). HeLa cells were from American Type Culture Collection (CCL-2™) and stored in the vapor phase of liquid nitrogen before use. Primary cell culture was completed with Dulbecco's Modified Eagle Medium with high glucose (DMEM, Gibco). Complete media was prepared with 10% foetal bovine serum (FBS; Wisent, Canada) and Pen-Strep (Sigma-Aldrich) supplementation. Trypan blue (Thermo Fisher) and Countess-3 instrumentation (Thermo Fisher) were used for cell counting. 2′,7′-Dichlorodihydrofluorescein diacetate and Amplex Red were purchased from Thermo Fisher and used without further purification. Lysis buffer for the amplex red assay was freshly prepared, containing 50 mM phosphate buffer (Sigma-Aldrich), 1 mM ethylenediaminetetraacetic acid (BioShop) and 0.5% Triton X-100 (Sigma-Aldrich). Detection buffer for the Amplex Red assay was freshly prepared (50 mM phosphate buffer pH 6.0 (Bioshop), 50 µM Amplex Red (Thermo Fisher) and 0.1 U

Alana Ogata joined the University of Toronto in 2021, appointed in the Department of Chemistry and the Department of Chemical and Physical Sciences at UTM. Alana completed her PhD as a NSFGFRP fellow with Dr Reginald Penner and a postdoctoral fellowship with Dr Joe Patterson at UC Irvine, and a NIH T32 postdoctoral fellowship at the Brigham and Women's Hospital with Dr David Walt. Dr Ogata now leads a research program centered on the development of nanomaterials and advanced diagnostic technologies using a new patient-centered approach, with focus on women's health such as endometriosis and menstrual-blood-based diagnostics.

Alana F. Ogata

mL^{-1} horseradish peroxidase (Sigma-Aldrich)). Cell survivability was determined using Cell Titre Blue assay (Promega).

Methods

Synthesis of PAA@BSA@c-ZIF-8

PAA@BSA@c-ZIF-8 was prepared with reference to our previous publication.[34] Briefly, solutions of 20 mM Zn(OAc)$_2$·2H$_2$O and 1400 mM 2-methylimidazole (2-mi) were prepared. 200 mg of BSA was dissolved in 10 mL of the 1400 mM 2-mi solution. Then, PAA was added to the solution. Next, the pH of the solution was adjusted to 10.2–10.5. Finally, 10 mL of Zn(OAc)$_2$·2H$_2$O (20 mM) was combined with the BSA-2-mi solution and allowed to react overnight. PAA@BSA@c-ZIF-8 nanoparticles were isolated by centrifugation. PAA@BSA@c-ZIF-8 nanoparticles was redispersed in MilliQ water.

Synthesis of ZIF-8

Two aqueous precursor solutions were prepared prior to synthesis. To achieve the desired molar ratio (35 : 1), 10 mL of 1400 mM 2-mi and 10 mL of 40 mM Zn(OAc)$_2$·2H$_2$O were combined in a glass scintillation vial, resulting in a final Zn(OAc)$_2$·2H$_2$O concentration of 20 mM. The vial was left to incubate at room temperature for 24 hours before being collected by centrifugation and dried at room temperature.

Fluorescence quenching and stern volmer calculations for BSA binding affinity to Cu and Fe

A standard solution of BSA at 10 mg mL^{-1} was used for quenching experiments. 0.1–1 mM of the metal was added, and fluorescence quenching was monitored at 340 nm. Langmuir isotherms were calculated using GraphPad Prism's Langmuir isotherm package. K_a values were calculated with Stern Volmer's equation. Electrophoretic light scattering measurements were taken for each metal-BSA mixture. Experiments are run in triplicate.

Synthesis of PAA@CuBSA@c-ZIF-8 and PAA@FeBSA@c-ZIF-8

PAA@CuBSA@c-ZIF-8 and PAA@FeBSA@c-ZIF-8 were prepared with reference to our previous publication.[34] 200 mg BSA was dissolved in MilliQ water, then CuCl$_2$ and FeCl$_3$ were added (0.5 mM), finally 1.14 g (1400 mM) of 2-mi was allowed to dissolve in the solution. Then, PAA was added to the solution. Next, the pH of the solution was adjusted to 10.2–10.4. Finally, 10 mL of Zn(OAc)$_2$·2H$_2$O (20 mM) was reacted with the BSA-2-mi solution and allowed to react overnight. The samples were centrifuged to isolate the particles. The particles were redispersed in MilliQ.

Catalytic activity screening

Catalytic screening of PAA@BSA@c-ZIF-8, PAA@CuBSA@c-ZIF-8 and PAA@FeBSA@c-ZIF-8 was completed using the TMB assay. 100 μM TMB, 10× diluted nanoparticles and 40 μM peroxide were added to a cuvette. The colorimetric response was measured after 1 hour at 37 °C. The buffer used in each case was pH 6.0 1× PBS. Colorimetric response was determined using a Nanodrop One C UV-Vis spectrophotometer at 652 nm (Thermo Fisher, USA). Experiments were run in triplicate.

Determination of protein encapsulation efficiency

Encapsulation efficiency (EE%) was determined using the Bradford assay. The supernatant from the mother reaction was obtained to measure the concentration of unreacted protein. EE% is determined with eqn (1)

$$\begin{aligned} EE_{SN}\% = ((\text{quantity of protein used in reaction} \\ - \text{ quantity of protein found in supernatant})/ \\ \text{quantity of protein used in reaction}) \times 100 \end{aligned} \quad (1)$$

Bradford measurements were taken on Nanodrop One C UV-Vis spectrophotometer at 595 nm (Thermo Fisher, USA). Experiments were run in triplicate.

Protein release curves

Protein release was monitored *via* the Bradford assay. First, the as-prepared samples were washed three times with MilliQ water (<18.2 Ω). The samples were redispersed in 1× PBS pH 6.0 with 40 μM hydrogen peroxide. Over the course of 6 hours the release of BSA was monitored by Bradford assay. Bradford measurements were taken on a Nanodrop One C UV-Vis spectrophotometer (Thermo Fisher, USA). Experiments are run in triplicate on two batches, for a total of $n = 6$, whole batches ($1 \times 10^{12} \pm 1 \times 10^{11}$ particles) were used for this experiment.

Circular dichroism (CD) spectroscopy

100 μL of metal-doped BSA before and after release was applied to a size exclusion column (Superdex 200, GE Healthcare, USA) on an AKTA FPLC (Cytiva, USA) in 20 mM Na$_3$PO$_4$, pH 7.2, and 150 mM NaCl, at a flow rate of 0.5 mL min^{-1}, fractions were collected in 0.5 mL increments.

Fractions containing BSA were determined by SDS-PAGE analysis and collected. 20 μL of the samples before SEC and each fraction was added to 5 μL of 5× SDS loading dye. 5 μL of SeeBlue™ Plus2 Protein Ladder, 5 μL of samples before SEC, and 10 μL of each fraction was applied to a 15% polyacrylamide gel. SDS-PAGE was performed with Tris-Glycine-SDS running buffer for 50 min at 180 V using BioRAD PowerPac Basic power supply and Mini-PROTEAN Tetra vertical electrophoresis cell. Protein concentration was determined by the Bradford assay and prepared for CD spectroscopy.

CD spectroscopy samples were generated by diluting BSA to 2 μM using buffer lacking NaCl (20 mM Na$_3$PO$_4$, pH 7.2) for a final NaCl concentration of less than 30 mM. All CD measurements were conducted in a 250 μL, 0.1 cm path length quartz cuvette.

CD Spectra were recorded at 22 °C from 190–260 nm with a 0.5 nm step size, bandwidth of 1 nm, scanning speed of 100 nm min^{-1} and a digital integration time of 4 s. Three scans are averaged for each CD spectra. Spectra were taken on a JASCO J-1500 CD spectrometer.

Mean residue ellipticity (MRE) values were calculated using eqn (2).

$$\text{MRE} = ((A - A_{\text{buffer}})/10(l)[\text{BSA}](n)) \tag{2}$$

where A is the absorbance at a given wavelength, A_{buffer} is the absorbance of the buffer without BSA, l is the pathlength of the cuvette, $[\text{BSA}]$ is the concentration of BSA in mol L^{-1} and n is the number of amino acid residues in BSA (583).

Alpha helical content of BSA was calculated using eqn (3).

$$\% \text{ Helix} = (\theta_{222}/-39\,500(1-(257/n))) \tag{3}$$

where θ_{222} is the MRE of BSA at 222 nm, $-39\,500$ is the theoretical MRE of a perfect helix at 222 nm, and n is the number of residues in BSA (583).

Powder X-ray diffraction measurements (XRD)

20 mL of washed PAA@BSA@c-ZIF-8, PAA@CuBSA@c-ZIF-8 and PAA@FeBSA@c-ZIF-8 was allowed to dry under vacuum for 4 hours. The sample was then powdered using a pestle and mortar. Approximately 50 mg of dry PAA@BSA@c-ZIF-8, PAA@CuBSA@c-ZIF-8 or PAA@FeBSA@c-ZIF-8 was placed on an amorphous silicon wafer and X-ray diffractograms were acquired using a D2 phaser with a Cu Kα (1.5406 Å) X-ray source (Bruker, Germany).

Fourier transform infrared spectroscopy (FTIR)

20 mL of as-prepared PAA@BSA@c-ZIF-8, PAA@CuBSA@c-ZIF-8 or PAA@FeBSA@c-ZIF-8 was allowed to dry under vacuum for 4 hours. The sample was then powdered using a pestle and mortar. Approximately 1 mg of dry PAA@BSA@c-ZIF-8, PAA@CuBSA@c-ZIF-8 or PAA@FeBSA@c-ZIF-8 was placed on the diamond and analysed. The FTIR used was a Nicolet iS20 (Thermo Fisher, USA).

ζ Potential

750 μL of post-wash nanoparticles (10-fold diluted) were placed in a DS1070 folded capillary zeta cell (Malvern Panalytical, USA). Each sample was allowed to equilibrate to 25 °C before measurement and was measured in triplicate. All electrophoretic light scattering measurements were acquired with a Zetasizer Nano series ZS (Malvern Panalytical, USA).

Dynamic light scattering (DLS)

For DLS, 1 mL of washed, 10-fold diluted, PAA@BSA@c-ZIF-8, PAA@CuBSA@c-ZIF-8 or PAA@FeBSA@c-ZIF-8 were redispersed in MilliQ water and monitored by DLS in a quartz cuvette. Each sample was allowed to equilibrate to 25 °C before measurement and was recorded in triplicate. All dynamic light scattering measurements were acquired with a Zetasizer Nano series ZS (Malvern Panalytical, USA). For PBS stability trials, PAA@BSA@c-ZIF-8, PAA@CuBSA@c-ZIF-8 and PAA@FeBSA@c-ZIF-8 were redispersed in 1× PBS pH 6.0. Experiments were run in triplicate.

Nanoparticle tracking analysis (NTA)

PAA@BSA@c-ZIF-8, PAA@CuBSA@c-ZIF-8 and PAA@FeBSA@c-ZIF-8 were washed three times and analysed at SickKids, Toronto, Ontario. The NTA apparatus used was NS300 NTA (Malvern Panalytical, USA). Samples were diluted 1500-fold prior to measurement and were recorded in triplicate.

Scanning electron microscopy (SEM)

As-prepared PAA@BSA@c-ZIF-8, PAA@CuBSA@c-ZIF-8 or PAA@FeBSA@c-ZIF-8 nanoparticles were diluted 1000-fold. Then, 40 μL of the diluted nanoparticles were drop-casted onto gold-coated glass. The gold-coated glass was adhered to the aluminium stub with carbon paint and carbon tape. The sample was allowed to dry on the glass and was coated with gold again. The samples were imaged with a SU3500 SEM (Hitachi, Japan). The working distance ranged from 4 mm–6 mm. The accelerating voltage ranged from 1 kV–25 kV.

Transmission electron microscopy (TEM)

For TEM, 100-fold diluted samples of PAA@BSA@c-ZIF-8, PAA@CuBSA@c-ZIF-8 and PAA@CuBSA@c-ZIF-8 were drop cast onto a lacey carbon film with a 200-mesh grid and 5 μm hole size (Electron Microscopy Sciences, USA). The grids were imaged using a Hitachi HT7700 TEM (Hitachi, Japan) at an accelerating voltage of 100 kV.

X-ray photoelectron spectroscopy (XPS)

Samples were prepared and analysed in agreement with our previous method.[35] Approximately 5 mg of dried PAA@BSA@c-ZIF-8, PAA@CuBSA@c-ZIF-8 or PAA@FeBSA@c-ZIF-8 was placed on the sample stage for analysis. An Al K-α source was used. Survey spectra were acquired at a pass energy of 200 eV. The corresponding point density on the energy axis was 1 eV per step. These scans were used to identified all elemental species in the PAA@BSA@c-ZIF-8 and PAA@CuBSA@c-ZIF-8 and PAA@FeBSA@c-ZIF-8 nanoparticles. Thermo Fisher's Avantage software was used to process the data. Data was obtained at the OCCAM Facility in Toronto, ON., Canada, using a K-α XPS system (Thermo Fisher, USA).

Inductively coupled plasma – atomic emission spectroscopy (ICP-AES) experiments – Zn, Cu and Fe incorporation rates

First, 1 mL of as-prepared PAA@BSA@c-ZIF-8, PAA@CuBSA@c-ZIF-8 and PAA@FeBSA@c-ZIF-8 were isolated and washed as previously described and redispersed in 1 mL of MilliQ water. Next, 1 mL of 70% metal-free HNO_3 was mixed with the redispersed nanoparticles. The samples were allowed to incubate for 48 hours before being diluted to 35 mL total volume. Ion release profile was monitored *via* collecting the supernatant of nanoparticles incubated with H_2O_2. First, the as-prepared samples were washed three times with MilliQ water (<18.2 Ω). The samples were redispersed in PBS pH 6.0 with 40 μM H_2O_2. Fractions of the supernatant were collected over 6 hours and mixed 1 : 1 v/v with 70% HNO_3 and later

diluted to 2% with MilliQ for ICP-AES analysis with an iCAP6500 Duo ICP-AES (Thermo Fisher, USA).

Cationic release rates

To determine the cationic release rates of Zn, Cu and Fe nanoparticles were reacted with 20, 40, 100 and 500 μM H_2O_2 and the release of ions was monitored by ICP-AES. Release rates were estimated using linear regression from the first 90 minutes of release. To assess cationic release, an entire batch was used.

Cell survivability assay

Approximately 5000 HeLa cells were seeded into each well of a 96-well plate with a final volume of 50 μL. Cells were allowed to grow for 24 hours in the incubator (37 °C, 5% CO_2) before being incubated with treatment. On each plate 12 controls (non-treatment samples) were prepared. The range of nanoparticle concentrations was 3×10^9–7×10^{10} particles per mL. Nanoparticle concentration was initially calculated using NTA. PAA@BSA@c-ZIF-8, PAA@CuBSA@c-ZIF-8 and PAA@FeBSA@c-ZIF-8 were redispersed in 10% FBS DMEM Media at 2× the required concentration. Then, 50 μL of the DMEM-NP solution, at the specified particle concentrations, were added to each well and incubated for 24 hours. Finally, 20 μL of Cell Titre Blue was added and incubated for one hour prior to measurement. Fluorometric response was collected on a Spark® Multimode Microplate Reader (Tecan, Switzerland) with an excitation value of 560 nm and emission value of 590 nm. Cell viability was determined *via* eqn (4). IC_{50} values were calculated on a particle per mL basis with GraphPad Prism.

$$\text{Cell viability\%} = ((\text{control response} - \text{treatment response})/ \\ \text{control response}) \times 100 \tag{4}$$

Measurement of intracellular ROS generation

The level of intracellular ROS generation was estimated using the 2,7′-dicholorodihydrofluorescein diacetate (DCF-DA) dye. We followed the protocol by Dhawan *et al.*[36] Briefly, cells were seeded at a density of 10^5 cells per mL and allowed to grow for 24 hours. Then, DMEM-particle solutions standardized to 1×10^{10} particles were added to each well (1 : 1 v/v). The plates were allowed to incubate in 37 °C, 5% CO_2 for 45 minutes upon which time the reaction mixture was replaced with 1× PBS pH 7.4 and measured on a microplate reader with excitation wavelength of 485 nm and emission wavelength of 528 nm. The fluorescence intensity was monitored and -fold change compared to controls was reported.

Determination of cellular peroxide levels pre- and post-incubation with nanoparticles

Cells were grown, harvested, and treated as normal. Then, 200 μL of lysis buffer (50 mM phosphate buffer pH 6.0, 0.5% Triton X-100, 1 mM ethylenediaminetetraacetic acid) was

added per 500 000 cells and homogenized. After homogenization, the samples were centrifuged at 14 000 rpm for 5 minutes. The supernatant was collected, and pellet was discarded. Then 50 μL of sample was added to each well with 100 μL of detection matrix (50 mM phosphate buffer pH 6.0, 50 μM Amplex Red and 0.1 U mL^{-1} HRP). The A560 response was recorded with Spark® Multimode Microplate Reader (Tecan, Switzerland) and compared to a calibration curve for cellular peroxide determination. The same process was completed with the addition of 1×10^{10} PAA@BSA@c-ZIF-8, PAA@CuBSA@c-ZIF-8 or PAA@FeBSA@c-ZIF-8 to evaluate the effect of nanoparticle concentration on intracellular peroxide concentration.

Replication of nanoparticle synthesis

A standard operating procedure was provided to additional operators to replicate the synthetic regime provided above. The standard operating procedure can be found in the electronic SI. For scaled synthesis of the PAA@BSA@c-ZIF-8, PAA@CuBSA@c-ZIF-8 and PAA@FeBSA@c-ZIF-8 synthesis, weights and volumes were increased by 25-fold with no other adjustments (20 mL to 500 mL).

Nitrogen gas absorption

Prior to preforming gas adsorption measurements, each sample was activated at 70 °C for 6 hours under dynamic vacuum (5×10^{-3} mbar) on the Schlenk line. For each measurement, 20–35 mg of the activated MOF was placed in a pre-weighed sample tube. The mass of the sample was recorded, and the tube was fitted with a glass rod and a cap. The samples were then activated on the instrument for 1 hour at 70 °C prior to measurement. Nitrogen gas isotherms were acquired using the Belsorp-miniX porosimeter at 77 K with N_2 and He. The Brunauer–Emmett–Teller (BET) surface areas were fitted using the software supplied with the instrument; BET consistency criteria were met for all samples.[37]

Statistical analysis

Statistical analysis for hypothesis testing in this work used the Brunner-Munzel *t*-Test calculated by GraphPad's Prism to a 95% confidence interval. Results were reported as exact *p*-values. For full width at half mass, values was calculated with the Cauchy-Lorentz function with a minimum R^2 of 0.9.

Results and discussion

Developing peroxide responsive nanoparticles based on BSA@c-ZIF-8

In early 2024, our group published the synthesis of colloidally stable BSA@c-ZIF-8 nanoparticles that were resistant to hydrolytic and buffer induced degradation.[34] Here, we expanded on our previous design and incorporated Cu or Fe in the BSA@c-ZIF-8 particles to include ions capable of undergoing Fenton-like chemistry and stimuli reponsive disassembly.

We aimed to introduce Cu and Fe catalytic sites while maintaining the following material properties of BSA@c-ZIF-8: (1) a monodisperse profile (PDI <0.2), (2) a monomodal distribution, (3) at least −30 mV ζ potential, (4) colloidally stable in relevant buffers, and (5) catalytically active toward H_2O_2. We assessed these properties for several synthetic conditions and excluded nanoparticle designs that did not meet the criteria (Scheme S1). If more than one design had all attributes, the nanoparticle with maximal protein encapsulation was used.

To incorporate Cu/Fe ions into the particles, we first pre-associated Cu and Fe with BSA, which is known for its strong metal-binding properties (SI Fig. S1).[38–44] The resulting CuBSA@c-ZIF-8 and FeBSA@c-ZIF-8 nanoparticles exhibited poor colloidal stability in PBS after 24 hours (PDI_{24} = 0.3 ± 0.2, 0.5 ± 0.2, SI Fig. S2) and near-neutral ζ potentials of −8 ± 3 mV and 0 ± 2 mV, respectively (SI Table S1). This was ascribed to surface charge screening by the Cu and Fe ions.[45,46] To improve surface charge and colloidal stability, we co-loaded PAA, which was previously demonstrated to improve stability in ZIF-8 systems.[47–49] We tested PAA concentrations from 0–250 mg and found that 10, 25, 50, 100, and 250 mg PAA exhibited ζ potential values below −30 mV and catalytic activity towards H_2O_2 (SI Table S1 and Fig. S6). Bradford assay indicated 50 mg PAA enabled the highest protein loading. The final synthesis conditions of 10 mM $Zn(OAc)_2 \cdot 2H_2O$, 1400 mM 2-mi, 10 mg mL^{-1} BSA, 0.5 mM Cu or Fe with 50 mg PAA (2 k M_n), pH 10.3 produced colloidally stable PAA@CuBSA@c-ZIF-8 with a size of 180 ± 20 nm, PDI = 0.1 ± 0.1 and ζ potential of −50 ± 10 mV and PAA@FeBSA@c-ZIF-8 with a size of 210 ± 20 nm, PDI = 0.1 ± 0.1 and ζ potential of −50 ± 10 mV (SI Fig. S5 and Table S1) and were studied for the remainder of this work. A summary of all nanoparticles prepared during this work is provided in Table S1.

XPS was used to confirm Cu and Fe integration in PAA@CuBSA@c-ZIF-8 and PAA@FeBSA@c-ZIF-8, respectively (Fig. 1a–c). In agreement with ZIF-8, we found a split Zn 2p peak at *ca.* 1025 eV and 1045 eV.[50] O 1s is observed at *ca.* 533 eV, which is ascribed to carboxyl groups present in the BSA.[50] C 1s was ascribed to the carbon in the 2-mi ligand, BSA, and adventitious carbon.[50] N 1s was observed at *ca.* 400 eV and corresponds to amines from the BSA and the nitrogenous groups in 2-mi.[50] Fe 2p1/2 and Fe 2p3/2 signals were found at *ca.* 710 eV and 730 eV (ref. 51) for PAA@FeBSA@c-ZIF-8, while for PAA@CuBSA@c-ZIF-8 Cu signals were found at *ca.* 935 eV and *ca.* 952 eV.[52] Cl 2p peaks were also found in the *ca.* 200 eV region, derived from the counter ions in the Cu and Fe precursors.

We confirmed the crystal structure of PAA@BSA@c-ZIF-8, PAA@CuBSA@c-ZIF-8 and PAA@FeBSA@c-ZIF-8 by comparing our diffractograms to a simulated *sod*-ZIF-8 diffractogram (COD card: 4118891). X-ray diffraction peaks corresponded to 8, 11, 13, 15, 17, 19, 25, and 27° 2θ matching Miller planes (011), (002), (112), (022), (013), (222), (114), and (134), respectively (Fig. 1d). The integration of cationic species showed no impact on the crystallinity of PAA@CuBSA@c-ZIF-8 and PAA@FeBSA@c-ZIF-8 when compared to PAA@BSA@c-ZIF-8 as

the FWHM of the 8° 2θ diffraction peak varied by <10%. FTIR of PAA@BSA@c-ZIF-8, PAA@CuBSA@c-ZIF-8 and PAA@FeBSA@c-ZIF-8 retained characteristic ZIF-8 features, with new peaks at *ca.* 1680 and 1100 cm^{-1} confirming BSA encapsulation *via* amide signatures (Fig. 1e).[53]

SEM and TEM images of the PAA@BSA@c-ZIF-8, PAA@CuBSA@c-ZIF-8 and PAA@FeBSA@c-ZIF-8 nanoparticles revealed rough, spherical morphology, deviating from the rhombic dodecahedron particle shapes seen for ZIF-8, consistent with other PAA@ZIF-8 composites (Fig. 1f–h).[47,48] Interestingly, DLS and NTA results showed different size particle distributions (Fig. 1(i), (j) and Table 1). We attribute this difference to DLS over-representing the average hydrodynamic radius in the presence of rare, large particles.[54] To validate nanoparticle sizes, we manually measured the particles with ImageJ on SEM images and found the size distributions were consistent with NTA measurements.

The surface area of a pristine ZIF-8 (see methods section) was compared to PAA@BSA@c-ZIF-8, PAA@CuBSA@c-ZIF-8 and PAA@FeBSA@c-ZIF-8 by fitting to the BET model. The BET surface area of pristine ZIF-8 was 1680 $m^2\ g^{-1}$, while for PAA@BSA@c-ZIF-8, PAA@CuBSA@c-ZIF-8 and PAA@FeBSA@c-ZIF-8 the surface area was 650 $m^2\ g^{-1}$, 640 $m^2\ g^{-1}$ and 670 $m^2\ g^{-1}$, respectively (SI Fig. S7). The loss in surface area seen in these samples is in good agreement with BSA@ZIF-8 materials presented by Gao *et al.* at 740 $m^2\ g^{-1}$ and Chen *et al.* at 730 $m^2\ g^{-1}$.[55,56] Mechanistically, this reduction is attributed to the BSA or PAA occluding pores, lowering total surface area.[57]

We determined the ζ potential of the PAA@BSA@c-ZIF-8, PAA@CuBSA@c-ZIF-8 and PAA@FeBSA@c-ZIF-8 with electrophoretic light scattering (ELS). To confirm PAA inclusion we compared the ζ potential of the non-PAA samples (CuBSA@c-ZIF-8, FeBSA@c-ZIF-8) to PAA@BSA@c-ZIF-8, PAA@CuBSA@c-ZIF-8 and PAA@FeBSA@c-ZIF-8 nanoparticles. For non-PAA samples the ζ potentials were 0 ± 2 mV for FeBSA@c-ZIF-8 and −8 ± 3 mV for CuBSA@c-ZIF-8 and −35 mV ± 3 mV for BSA@c-ZIF-8 but improved in all cases for the pH controlled PAA synthesis to −50 ± 10 mV, ascribed to the COO^- moieties on PAA (Fig. 1k). We regard this shift as evidence of PAA's incorporation to the nanoparticle, as well as a positive benchmark for colloidal stability by overcoming the |30 mV| threshold to prevent particle to particle interactions.[58,59]

Protein release from PAA@BSA@c-ZIF-8, PAA@CuBSA@c-ZIF-8 and PAA@FeBSA@c-ZIF-8

We hypothesized that PAA@CuBSA@c-ZIF-8 and PAA@FeBSA@c-ZIF-8 would exhibit protein release driven by Fenton-mediated radical degradation. To evaluate this hypothesis, we incubated PAA@BSA@c-ZIF-8, PAA@CuBSA@c-ZIF-8 and PAA@FeBSA@c-ZIF-8 with 40 μM H_2O_2 over 6 hours and monitored BSA release using both the Bradford assay and DLS. PAA@BSA@c-ZIF-8, PAA@CuBSA@c-ZIF-8 and PAA@FeBSA@c-ZIF-8 demonstrated protein release (Fig. 2a). However, PAA@BSA@c-ZIF-8 samples had the lowest protein release at 100 ± 60 μg mL^{-1} over the 6 hours (n = 6, two
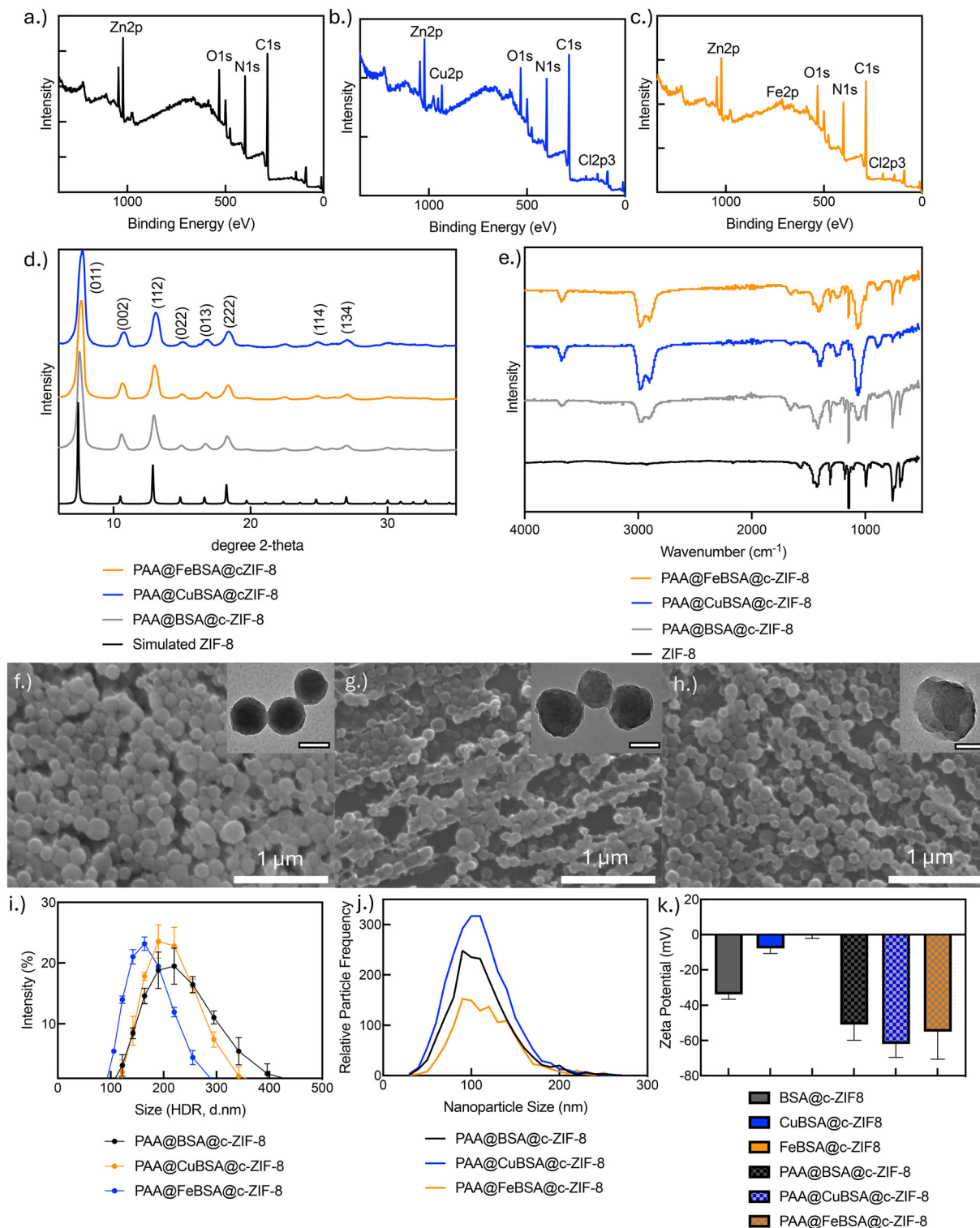
Fig. 1 Describes the physical characterization of PAA@BSA@c-ZIF-8, PAA@CuBSA@c-ZIF-8 and PAA@FeBSA@c-ZIF-8. (a–c) Show the X-ray photo-electron spectroscopy survey spectrum of PAA@BSA@c-ZIF-8, PAA@FeBSA@c-ZIF-8 and PAA@CuBSA@c-ZIF-8. (d) Shows the X-ray diffractograms of each nanoparticle, a *sod*-ZIF-8 simulated diffractogram is also provided (COD: 4118891). The miller indices are labelled above each peak diffraction plane. The FTIR spectra of each nanoparticle are shown in (e) with a control ZIF-8 sample for comparison. (f), (g) and (h) show scanning electron micrographs for each nanoparticle, PAA@BSA@c-ZIF-8, PAA@CuBSA@c-ZIF-8 and PAA@FeBSA@c-ZIF-8, respectively, with high-resolution TEM images provided in the inset of each SEM micrograph. The scale bar for the TEM images is 100 nm. (i) and (j) show the size distribution of the nanoparticles as calculated by DLS and NTA, respectively (n = 3). Each point and associated error represent the average and standard deviation of 3 measurements, respectively (k) shows the zeta potential of all three nano-species (n = 3) with and without added PAA. Each point and associated error represent the average and standard deviation, respectively.

Table 1 Summary of the sizes recorded *via* DLS, NTA and physical measurements. DLS $n = 3$, NTA $n = 3$, physical size $n = 50$ particles with ImageJ on scanning electron micrographs of each particle

Particle	Size (DLS)	Size (NTA)	Size (SEM)
PAA@BSA@c-ZIF-8	200 ± 20 nm	130 ± 10 nm	140 ± 20 nm
PAA@CuBSA@c-ZIF-8	180 ± 20 nm	120 ± 10 nm	110 ± 10 nm
PAA@FeBSA@c-ZIF-8	210 ± 20 nm	140 ± 10 nm	120 ± 30 nm
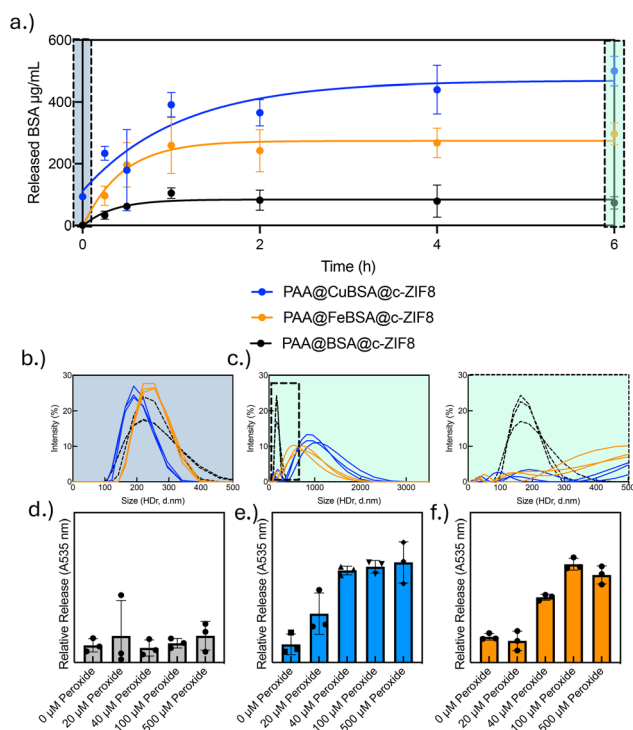
Fig. 2 Protein release of PAA@BSA@c-ZIF-8, PAA@CuBSA@c-ZIF-8 and PAA@FeBSA@c-ZIF-8 nanoparticles. (a) Shows the protein release from PAA@BSA@c-ZIF-8, PAA@CuBSA@c-ZIF-8, PAA@FeBSA@c-ZIF-8. Each point and error bar represents the average and standard deviation of 6 data points across 2 batches, respectively (b) shows the DLS continuing distribution analysis plots without added peroxide (time = 0) (c), show the nanoparticles after 6 hour incubation with 40 μM peroxide. (d) The solid black box shows the size range from 0–3000 nm, while the dotted box is a zoomed in portion (corresponding to the dotted black box) of 0–500 nm to highlight the smaller peaks. (e–g) Represent the relative protein release as a function of H_2O_2 (one batch in triplicate) from PAA@BSA@c-ZIF-8 (c), PAA@CuBSA@c-ZIF-8 (d) and PAA@FeBSA@c-ZIF-8 (e). All analyses were performed in 1× PBS pH 6.0. Each point and associated error represent the average and standard deviation of 3 measurements, respectively.

batches in triplicate), whereas the PAA@CuBSA@c-ZIF-8 and PAA@FeBSA@c-ZIF-8 released 520 ± 90 μg mL^{-1} and 350 ± 80 μg mL^{-1} of BSA ($n = 6$, two batches in triplicate) over the same time period, respectively. After H_2O_2 exposure, the PAA@BSA@c-ZIF-8 structure was preserved with an average hydrodynamic radius of 210 nm ± 50 nm, in agreement with the size of PAA@BSA@c-ZIF-8 (Fig. 2b). However, when compared to the DLS measurements of PAA@CuBSA@c-ZIF-8 and

PAA@FeBSA@c-ZIF-8 after H_2O_2 incubation, we found the nanoparticles were degraded, evidenced by a variety of smaller structures (*ca.* 10 nm, *ca.* 50 nm) and large, 1000–2000 nm, aggregates on the continuing distribution analysis plots (Fig. 2b). We ascribed the large peaks to aggregated ZIF-8 material after disassembly, while the smaller peaks (10 nm and 50 nm) were ascribed to be free and aggregated BSA, respectively. To verify that catalytic activity of the PAA@CuBSA@c-ZIF-8 and PAA@FeBSA@c-ZIF-8 was not derived from free or loosely bound Cu and Fe ions leftover from synthesis, we incubated the nanoparticles in PBS without H_2O_2. We then separated the nanoparticles *via* centrifugation and to isolate any free Cu or Fe ions in solution. We tested the catalytic activity of the supernatant and found that the activity was indistinguishable from baseline, suggesting that free Cu and Fe were not released in sufficient quantities in PBS alone to participate in Fenton's chemistry (SI Fig. S8).

To understand the effect of H_2O_2 on protein release, we tested H_2O_2 concentrations of 0, 20, 100, and 500 μM and show that increased H_2O_2 concentrations had no increased effect on releasing protein from PAA@BSA@c-ZIF-8. In contrast, the PAA@FeBSA@c-ZIF-8 nanoparticles showed an increase of 30 ± 10% BSA release at 100 μM H_2O_2 compared to 40 μM. PAA@CuBSA@c-ZIF-8 showed no increase in release of BSA beyond 40 μM H_2O_2 (Fig. 2c–e). We found that the released protein remained catalytically active toward H_2O_2, suggesting that released Cu/Fe-BSA complexes can generate ROS after release (SI Fig. S8 and S9). These findings demonstrate that Cu- and Fe-doped protein@ZIF-8 nanoparticles undergo Fenton-mediated disassembly in response to H_2O_2, enabling controlled protein release and sustained catalytic activity post-release.

The fraction of released protein from PAA@CuBSA@c-ZIF-8 and PAA@FeBSA@c-ZIF-8 over 6 hours was 21 ± 6% and 18 ± 4%, respectively ($n = 6$, 2 batches tested in triplicate), a release profile is comparable to other proteinaceous MOFs presented in literature. For example, green fluorescent protein release from ZIF-90 (Zn^{2+} nodes and imidazole-2-carboxaldehyde struts) was 6% under optimal conditions,[60] while 5–11% release of CRISPR-Cas9 was presented in PB@Eu-MOFs upon photothermal irradiation,[61] and 20% BMP-2 release was presented after 7 days in Lu's BMP-2/cisplatin derived nanoZIF-8.[62]

Ion release from PAA@BSA@c-ZIF-8, PAA@CuBSA@c-ZIF-8, and PAA@FeBSA@c-ZIF-8

To understand ion release profiles, we used ICP-AES to determine the total incorporation of zinc (Zn), Fe and Cu in PAA@BSA@c-ZIF-8, PAA@CuBSA@c-ZIF-8 and PAA@FeBSA@c-ZIF-8 (Table 2) and then evaluated the released fraction of each ion over 6 hours, with and without H_2O_2 present (Fig. 3).

In all H_2O_2-treated samples, we observed the release of Zn and Cu or Fe. For PAA@CuBSA@c-ZIF-8, 82 ± 3% of total Cu was released after 360 minutes, corresponding to 76 ± 12 μM Cu, along with 51 ± 11% of the total Zn, equivalent to 5.6 ±

Table 2 Summary of the zinc, copper and iron concentrations for the nanoparticle samples used in this work. $n = 9$, three batches ($1 \times 10^{12} \pm 2 \times 10^{11}$ nanoparticles) measured in triplicate

Nanoparticle sample	Zn (mM)	Cu (μM)	Fe (μM)
PAA@BSA@c-ZIF-8	10 ± 1	N/A	N/A
PAA@CuBSA@c-ZIF-8	11 ± 1	93 ± 4	N/A
PAA@FeBSA@c-ZIF-8	10 ± 1	N/A	45 ± 4

0.7 mM (Fig. 3b). Similarly, PAA@FeBSA@c-ZIF-8 released 64 ± 5% of total iron (29 ± 3 μM Fe) and 58 ± 4% of Zn, amounting to 5.7 ± 0.3 mM Zn (Fig. 3c). In contrast, PAA@BSA@c-ZIF-8 nanoparticles released 31 ± 3% of total Zn under identical conditions (Fig. 3a). These results indicate that the presence of Cu or Fe enhanced Zn release, suggesting catalytic degradation of the nanoparticles is mediated by Fenton chemistry in the presence of H_2O_2.

However, to test the efficacy of the ion release from PAA@CuBSA@c-ZIF-8 and PAA@FeBSA@c-ZIF-8 in serum containing media, the release of Cu and Fe was evaluated in DMEM fortified with 10% FBS. DMEM with serum is a more complex medium than PBS and more representative of a real sample. In agreement with the PBS samples, we found ion release in the DMEM samples (SI Fig. S10). The PAA@BSA@c-ZIF-8 showed Zn release was limited to 10% after 90 minutes. The PAA@CuBSA@c-ZIF-8 samples released 82 ± 2% of its Cu and 24 ± 3% of its Zn after 90 minutes. While the PAA@FeBSA@c-ZIF-8 samples released 46 ± 2% of its Fe and 29 ± 2% its Zn after 90 minutes. Interestingly, the release rate of Cu was increased in DMEM compared to PBS samples, but the Zn release rate was reduced. As well, in the PAA@FeBSA@c-ZIF-8 samples, the release rate of Fe and Zn was reduced compared to PBS. We hypothesized that released Fe and Zn created insoluble complexes with components in DMEM, and as a result were not observed by ICP-AES.

We additionally evaluated the release of PAA@CuBSA@c-ZIF-8 and PAA@FeBSA@c-ZIF-8 at 20, 100 and 500 μM H_2O_2 in PBS. We found that for PAA@CuBSA@c-ZIF-8, the rate of release increased as the concentration of H_2O_2 increases. However, the release rate of Fe decreased at 100 μM and 500 μM H_2O_2 while Zn increased. This data suggests that in the presence of higher concentrations of peroxide, Fe may have formed insoluble aggregates that are not observed by ICP-AES (SI Fig. S13).

### Structural characterization of released BSA

Protein confirmational changes induced by metal binding have been well documented in literature, thus we hypothesized that Cu- and Fe-binding, protein encapsulation and subsequent release would affect the secondary structure or oligomeric state of BSA.[63–65] SEC separates proteins based on hydrodynamic radii, allowing for separation of monomeric BSA and higher-order oligomers. We first applied unreacted BSA to a Superdex200 size exclusion column to evaluate the oligomeric state of the BSA before metal binding (Fig. 4a). The SEC chromatograms show multiple peaks and SDS-PAGE analysis was employed to assess which fractions contained BSA. We found that most of the sample was monomeric with an elution volume of 14 mL, which corresponded to 75 kDa in size. BSA is 66 kDa, but due to BSA's elongated structure, elution at a larger size was expected.[66] In addition to the BSA peak, there were low populations of oligomeric BSA and contaminating high molecular weight proteins in the BSA.

Secondary structure of BSA was then evaluated by CD spectroscopy (Fig. 4b). The CD spectra of BSA showed local minima at 208 and 222 nm, indicative of proteins with α-helices. Using equations 2 & 3 BSA's helical structure was calculated to be 55.6%. BSA is reported to contain 67% α-helix structure, however, secondary structure is affected by multiple factors, including pH, temperature, and solvent.[67,68] We also evaluated
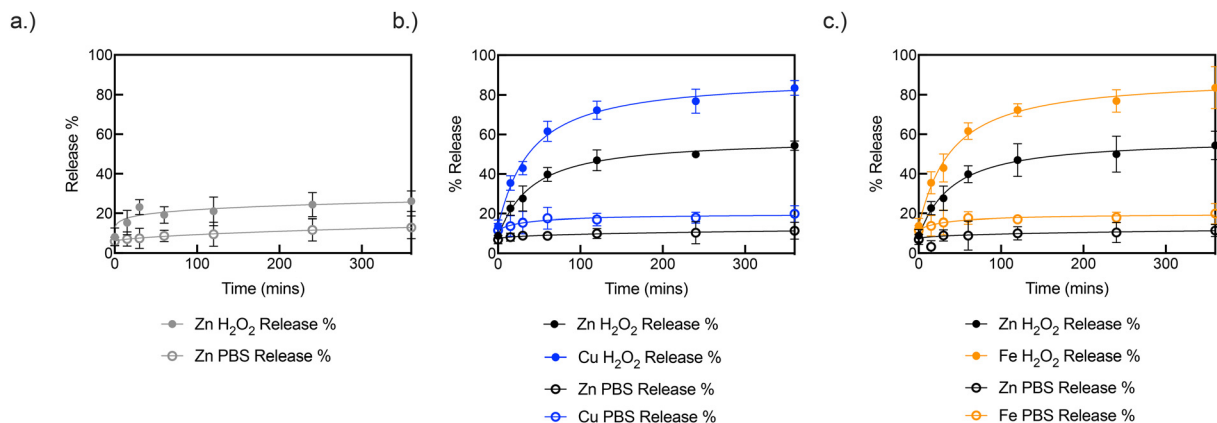
Fig. 3 The release profiles of each nanoparticle presented in this work. (a) Shows the release of Zn from PAA@BSA@c-ZIF-8 samples in the presence of 40 μM H_2O_2 compared to no peroxide. (b) Shows the release of copper and zinc in the same manner. (c) Shows the release of iron and zinc in the same manner. The spectral lines used were Zn {334.502}, Cu {327.396} and Fe {259.940}. All samples are $n = 3$, except for Fe $t = 60$ minutes, which was $n = 2$ due to instrument changeover. Each point and error represent the average and standard deviation of three measurements from one batch, respectively.
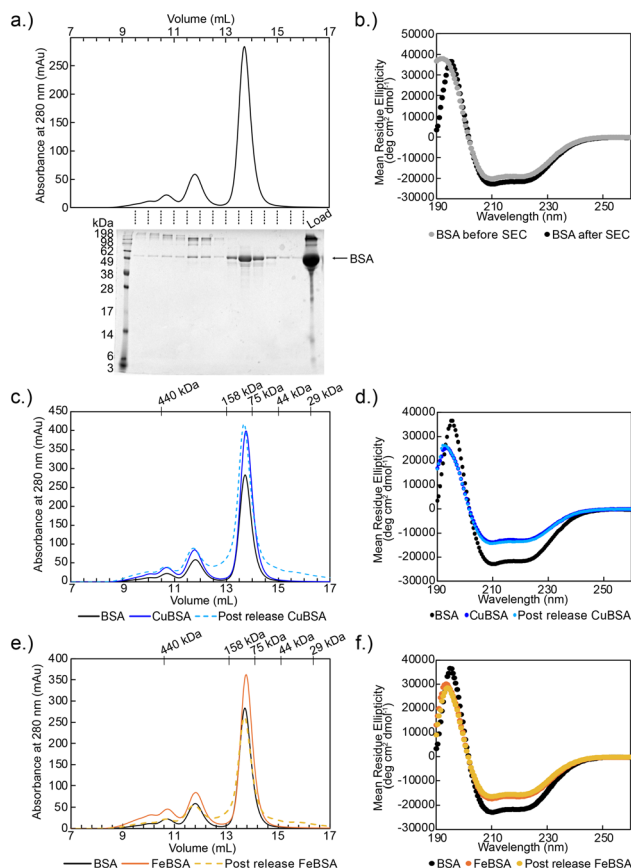
Fig. 4 Metal-doping decreases secondary structure of BSA. (a) S200 size exclusion trace of BSA and SDS-PAGE gel corresponding to the elution fractions. (b) CD spectra of BSA before and after size exclusion. (c) S200 size exclusion traces of BSA, CuBSA, and post release CuBSA. (d) CD spectra of BSA, CuBSA, and post release CuBSA. (e) S200 size exclusion traces of BSA, FeBSA, and post release FeBSA. (f) CD spectra of BSA, FeBSA, and post release FeBSA.

the secondary structure of BSA before purification by SEC and found that there was minimal change in secondary structure for BSA before and after SEC.

These experiments were repeated using CuBSA and FeBSA before and after protein encapsulation (Fig. 4c–f and SI Fig. S11). We found that the addition of Cu/Fe to BSA did not impact the oligomeric state of BSA. Further, we found that when Cu and Fe were bound to BSA the α-helical content decreases from 54.6% to 33.2% for CuBSA and to 41.2% for FeBSA. Similar results are shown for the post-release samples of Cu and FeBSA (Table 3).

We then assessed the impact of protein concentration on the oligomerization of BSA as application of PAA@BSA@c-ZIF-8, PAA@CuBSA@c-ZIF-8 and PAA@FeBSA@c-ZIF-8 are done at lower concentrations. SEC experiments were repeated using 0.2 mg mL^{-1} of ZnBSA, CuBSA, and FeBSA (SI Fig. S12). At this concentration, the BSA remained mostly monomeric, though some oligomers and contaminating proteins were still present.

Table 3 MRE and α-helical content of metal-doped BSA before and after nanoparticle encapsulation

	BSA	CuBSA	PRCuBSA[a]	FeBSA	PRFeBSA[a]
MRE at 222 nm (deg cm^2 dmol^{-1})	−21 050	−13 000	−13 500	−16 200	−15 400
% α-helix	54.6	33.2	34.3	41.2	39.3

[a] PR = post-release

This work showed that BSA remains monomeric after metal doping, nanoparticle encapsulation and release, however, the secondary structure of BSA decreased upon interaction with Cu and Fe. We additionally observed that the released BSA retains the decrease in secondary structure. We hypothesized that metal binding causes rearrangement within the protein, disrupting the secondary structure of BSA, and the structural impacts of this binding event are observed in the released protein.[63–65] The results of this study highlight the importance of understanding the secondary structure of the released protein from nanomaterials. Here, BSA does not serve an enzymatic function, but the efficacy of releasing active enzymes, like glucose oxidase or carbonic anhydrase may be affected by the metal-associated approach described herein.

Nanoparticle stability

We then tested if our nanoparticles could be stored for a short period (14 days) prior to use to accommodate for storage and shipping times. The stability of PAA@BSA@c-ZIF-8, PAA@CuBSA@c-ZIF-8 and PAA@FeBSA@c-ZIF-8 was assessed in water (7.1 pH), PBS (1×, 7.4 pH), HEPES (25 mM, 8.0 pH) and complete DMEM at a concentration of $1 \times 10^{12} \pm 2 \times 10^{11}$ nanoparticles. All nanoparticles were colloidally stable by our previously established metrics (SI Fig. S13).[34] Additionally, we evaluated the release of cations after 1, 3, 5 and 7 days of storage in DMEM 10% FBS to evaluate if release was compromised during storage (SI Fig. S14). We extracted the linear region of the cation release and used linear regression to calculate the release rate (Table 4). Further, we calculated the total quantity of cation released at t = 360 min (Table 4). PAA@CuBSA@c-ZIF-8 showed a Cu release rate of 0.73 ± 0.12 μM/min after 1 day of storage in DMEM, but decreased to 0.56 ± 0.09 μM min^{-1} after 14 days of storage. PAA@FeBSA@c-ZIF-8 showed an Fe release rate of 0.21 ± 0.05 μM min^{-1} after 1 day of storage in DMEM but decreased to 0.18 ± 0.04 μM min^{-1} after 14 days. Both nanoparticles showed a decrease in t = 360 ion release.

We hypothesize that serum components in the DMEM form a protein corona on the nanoparticles, which can alter the release kinetics and the total release profile of both PAA@CuBSA@c-ZIF-8 and PAA@FeBSA@c-ZIF-8. Protein coronas are well known to alter nanoparticle release profiles *via* surface adsorption. When proteins are adsorbed, they can alter the surface chemistry of nanoparticles, impairing release or reducing reactivity, thereby compromising efficacy.[69–72] We

Table 4 Release rates of cations for the first 90 min ($r^2 > 0.95$) and total cation released at $t = 360$ minutes from PAA@CuBSA@c-ZIF-8, PAA@FeBSA@c-ZIF-8. $n = 9$ technical replicates

	Day 1	Day 3	Day 7	Day 14
PAA@CuBSA@c-ZIF-8 Cu release rate	0.73 ± 0.12 μM min^{-1}	0.71 ± 0.11 μM min^{-1}	0.65 ± 0.14 μM min^{-1}	0.56 ± 0.09 μM min^{-1}
PAA@CuBSA@c-ZIF-8 $t = 360$	86 ± 11 μM	82 ± 10 μM	72 ± 12 μM	70 ± 15 μM
PAA@FeBSA@c-ZIF-8 Fe release rate	0.21 ± 0.05 μM min^{-1}	0.20 ± 0.03 μM min^{-1}	0.20 ± 0.05 μM min^{-1}	0.18 ± 0.04 μM min^{-1}
PAA@FeBSA@c-ZIF-8 $t = 360$	26 ± 2 μM	26 ± 5 μM	24 ± 3 μM	20 ± 1μM

found that after 7 days in DMEM the 90 minute release rate was compromised for PAA@CuBSA@c-ZIF-8 and PAA@FeBSA@c-ZIF-8 (Table 4 and SI Fig. S15). Therefore, PAA@CuBSA@c-ZIF-8 and PAA@FeBSA@c-ZIF-8 nanoparticles dispersed in DMEM were used within 3 days.

Cell studies

The release of Zn, Cu, and Fe from the nanoparticles can be pro-apoptotic to cancerous cells *via* several well-established mechanisms. Cu and Fe are potent inducers of oxidative stress through the production of ROS due to their redox cycling capacity, leading to the production of hydroxyl radicals, causing lipid peroxidation, DNA damage, and protein denaturation.[3,4] Fe and Cu are also both closely involved in their name-sake apoptotic mechanisms, ferroptosis and cuproptosis.[73,74] Furthermore, Zn can inhibit antioxidant enzymes such as glutathione reductase and catalase, thereby impairing the cellular defence against reactive oxygen species.[75,76]

We analysed the cytotoxic effects of PAA@BSA@c-ZIF-8, PAA@CuBSA@c-ZIF-8 and PAA@FeBSA@c-ZIF-8 on HeLa cells using the Cell Titre Blue assay.[77] Nanoparticle concentrations were determined by NTA. The average particle counts ($n = 4$, 4 batches across 4 operators measured in triplicate) were found to be $1.1 \times 10^{12} \pm 3.6 \times 10^{11}$ particles per mL for PAA@BSA@c-ZIF-8, $1.0 \times 10^{12} \pm 1.7 \times 10^{11}$ particles per mL for PAA@CuBSA@c-ZIF-8 and $8.7 \times 10^{11} \pm 2.0 \times 10^{11}$ particles per mL for PAA@FeBSA@c-ZIF-8. Corresponding IC$_{50}$ values

against HeLa cells were calculated for each nanoparticle across three biological replicates (Fig. 5a). The IC$_{50}$ for PAA@CuBSA@c-ZIF-8 was 2.7×10^9 particles per mL, for PAA@FeBSA@c-ZIF-8 the IC$_{50}$ was, 4.0×10^9 particles per mL while PAA@BSA@c-ZIF-8 was 1.3×10^{10} particles per mL. The Cu and FeBSA variants of the nanoparticles are significantly more cytotoxic towards HeLa cells that the undoped variants of the nanoparticles ($p = 0.001$, $p = 0.003$, respectively, $n = 3$ biological replicates).

To understand the mechanism for cell death, we employed the DCF-DA assay. DCF-DA is an intracellular radical reporter that is cleaved to fluorescent DCF in the presence of ROS.[36] Cells incubated with PAA@BSA@c-ZIF-8 did not have a significant fold increase in DCF cleavage 1.2 ± 0.2 ($p = 0.24$), but a 1.9 ± 0.2 ($p = 0.007$) and 1.7 ± 0.2-fold ($p = 0.0004$) increase in DCF signal was realized for PAA@CuBSA@c-ZIF-8 and PAA@FeBSA@c-ZIF-8 incubated cells, respectively (Fig. 5b, $n = 9$, 3 biological replicates across three batches measured in triplicate). This data suggests that PAA@CuBSA@c-ZIF-8 and PAA@FeBSA@c-ZIF-8 nanoparticles increase intracellular ROS production compared to PAA@BSA@c-ZIF-8. For further validation, we determined the peroxide concentration in cells with and without nanoparticle treatment. Untreated cells presented with a peroxide concentration of 4.1 ± 0.4 μM, while those treated with PAA@BSA@c-ZIF-8 had a concentration of 3.1 ± 0.4 μM ($p = 0.06$). PAA@CuBSA@c-ZIF-8 and PAA@FeBSA@c-ZIF-8 treated cells had peroxide concentrations of 1.0 ± 0.1 μM ($p = 0.004$) and 2.8 ± 1.0 μM ($p = 0.12$), respectively (Fig. 5c, $n =$
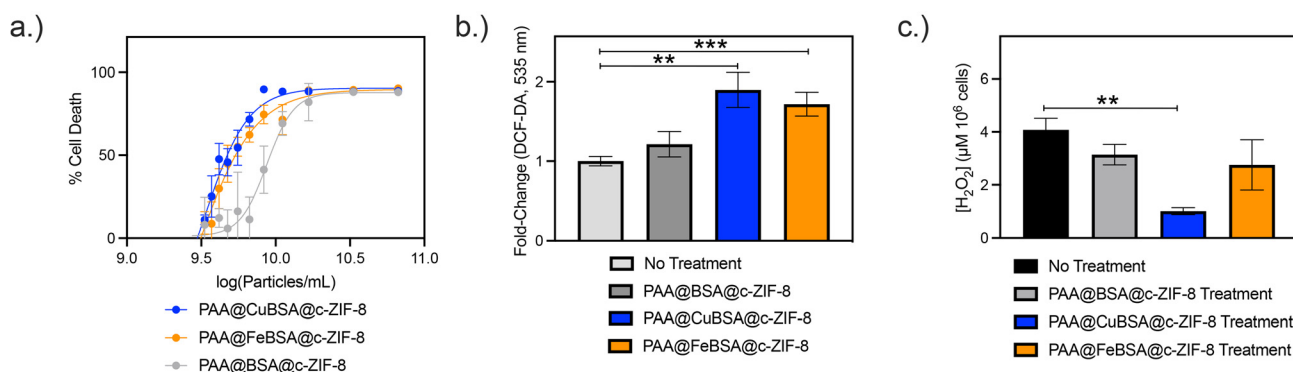
Fig. 5 Cell studies with the three selected nanoparticles. (a) Shows the % Cell Death curves and associated fit from which IC$_{50}$ values are calculated. ($n = 3$ biological replicates across three batches) (b) shows the fold-change for the DCF-DA assay. ($n = 9$, 3 biological replicates across three batches, measured in triplicate) (c) shows the concentration of peroxide after 24 hour incubation. For (c) measurements are normalized to 100 000 cells ($n = 9$, 3 biological replicates across three batches, measured in triplicate). Each point and error represent the average and standard deviation of three measurements from one batch, respectively.

9, 3 biological replicates tested against 3 batches measured in triplicate). This data is good evidence that the PAA@CuBSA@c-ZIF-8 and PAA@FeBSA@c-ZIF-8 nanoparticles caused peroxide depletion in the cells.[78]

Reproducibility and scaled synthesis of PAA@BSA@c-ZIF-8, PAA@CuBSA@c-ZIF-8, PAA@FeBSA@c-ZIF-8

Since the development of nanocarriers for active pharmaceutical ingredient delivery, reproducibility has been highlighted as principally important.[79–83] Thus, we evaluated the reproducibility of PAA@BSA@c-ZIF-8, PAA@CuBSA@c-ZIF-8 and PAA@FeBSA@c-ZIF-8 across four operators. To support this evaluation, we followed guidance from the U.S. Department of Health and Human Services, as well as Health Canada, which emphasize the assessment of critical quality attributes (CQAs) in therapeutic development.[84,85] CQAs are defined as measurable end-product characteristics that influence the safety, efficacy, or performance of a therapeutic. For the nanoparticles presented here, we categorized CQAs into three domains: physical properties (size, particle count, dispersity), chemical properties (ion incorporation, ζ potential), and therapeutic performance (IC_{50} values). This multivariate framework enables robust assessment of batch-to-batch consistency and facilitates the correlation of physiochemical attributes with material outcomes. We propose that early implementation of CQA-based evaluation is essential for ensuring reproducibility and improving regulatory readiness in both academic and industrial nanotechnology development.

Across 21 batches, the average size for PAA@BSA@c-ZIF-8 was 200 ± 20 nm, the size of PAA@CuBSA@c-ZIF-8 was 190 ± 20 nm, while PAA@FeBSA@c-ZIF-8 was 200 ± 20 nm, in agreement with the originally reported sizes (Fig. 6a–c, $n = 63$, 21 batches tested in triplicate). Maximal inter- and intra-operator variation was seen for PAA@BSA@c-ZIF-8 nanoparticles with a COV of 10%. We similarly evaluated the consistency of PAA@BSA@c-ZIF-8, PAA@CuBSA@c-ZIF-8 and PAA@FeBSA@c-ZIF-8 by ELS. The average ζ potential for the nanoparticles was -52 ± 5 mV for PAA@BSA@c-ZIF-8, -51 ± 6 mV for PAA@CuBSA@c-ZIF-8 and -52 ± 5 mV (Fig. 6d–f, $n = 63$, 21 batches tested in triplicate) in all cases the inter- and intra-operator COV was 10%. The PDI of all nanoparticle batches produced was below 0.2, suggesting the nanoparticles were consistently monodispersed (Fig. 6g–i, $n = 63$, 21 batches tested in triplicate).

While properties, such as size and ζ potential, can impact therapeutic properties,[85–91] guidance asserts that functional properties of the nanomaterial should be evaluated. Thus, we tested that the release and encapsulation of the ions/protein was consistent across operators (SI Fig. S16, across three operators and the author tested in triplicate, $n = 36$). The ion incorporation was consistent across operators and nanoparticles had a maximal inter- and intra-operator COV of 10% for all ions ($n = 12$, 4 batches across four operators tested in triplicate). As well, the ion release at $t = 360$ minutes is consistent with inter- and intra-operator COVs <20% across all ions and operators. The BSA release at $t = 360$ minutes for PAA@BSA@c-ZIF-8 was 120 ± 70 µg mL^{-1}, with a maximal inter-operator
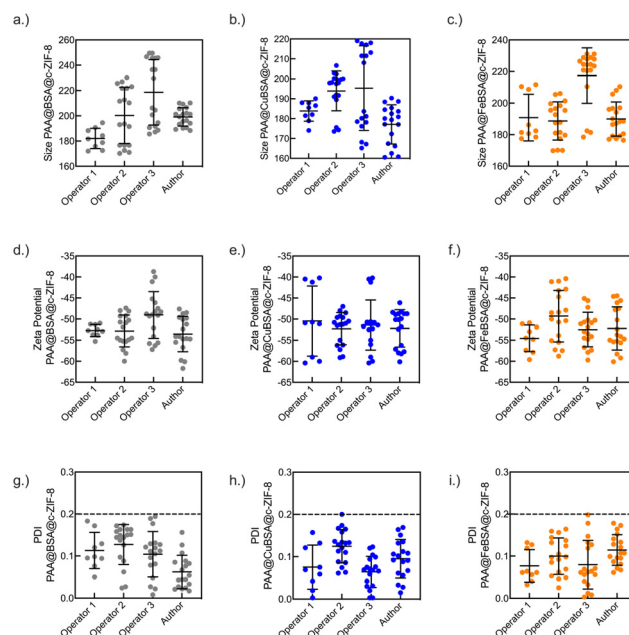
Fig. 6 Dot plots relating to the replication synthesis performed by four operators across various characterization techniques (operator 1: 3 batches measured in triplicate, $n = 9$, operator 2, 3 and author, 6 batches measured in triplicate, $n = 18$, in total 21 batches are tested for $n = 63$). (a–c) Shows the average size of the nanoparticles across three operators and the author. (d–f) Show the PDI values determined by DLS across three operators and the author (g–i) show the zeta potential results from electrophoretic light scattering across three operators and the author. Each dot represents one measurement. Error bars are provided representing the mean and standard deviation are provided for each data set.

COV of 40%. While for PAA@CuBSA@c-ZIF-8 and PAA@FeBSA@c-ZIF-8, 530 ± 90 µg mL^{-1}, and 400 ± 50 µg mL^{-1} of BSA was released with maximal COV of 20% for both inter- and intra-operators (SI Fig. S16, across three operators and the author tested in triplicate, $n = 36$).

Next, we sought to determine the consistency of the therapeutic response for the nanoparticles. Eight batches were selected, and we determined the IC_{50} and DCF-DA response for each nanoparticle. We found that in agreement with previous results, DCF-DA response for PAA@CuBSA@c-ZIF-8 and PAA@FeBSA@c-ZIF-8 increased by 1.8 ± 0.2 and 1.4 ± 0.1-fold, respectively, while PAA@BSA@c-ZIF-8 had a fold increase of 1.1 ± 0.1 (Fig. 7a–c, $n = 63$, 21 batches tested in triplicate) We found that across the four operators, the average IC_{50} values for the nanoparticles was $1.2 \times 10^{10} \pm 2.8 \times 10^9$ particles per mL, $3.2 \times 10^9 \pm 8.4 \times 10^8$, and, $5.0 \times 10^9 \pm 6.7 \times 10^8$ for PAA@BSA@c-ZIF-8, PAA@CuBSA@c-ZIF-8, and, PAA@FeBSA@c-ZIF-8, respectively, in agreement with the original batches tested (Fig. 7d–f, $n = 21$ across 21 batches).

Through the evaluation of these properties, we assessed the correlation between the physical properties and the effect the nanoparticles had on cell survivability. We hypothesized that DCF-DA response would directly correlate with cell death and show a negative correlation between DCF-DA response and the
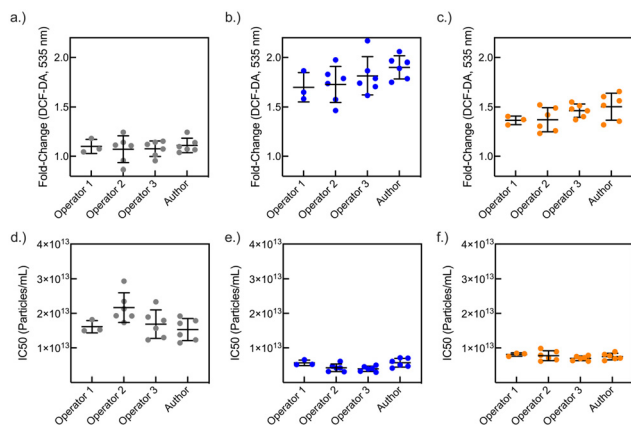
Fig. 7 Dot plots relating to the replication synthesis performed by four operators across various characterization techniques (operator 1: 3 batches measured in triplicate, $n = 9$, operator 2, 3 and author, 6 batches measured in triplicate, $n = 18$, in total 21 batches were tested.) (a–c) shows the change in DCF response compared to untreated samples. (d–f) Show the IC_{50} values determined by the Cell Titre Blue assay across three operators and the author. Each dot represents one measurement. In all cases, cell seeding density was 5×10^4 cells per mL. Error bars are provided representing the mean and standard deviation are provided for each data set.

resultant IC_{50} values (Fig. 8a–c), highlightingDCF-DA response as a critical quality metric used to measure consistency across batches and operators. We were unable to establish correlations between cytotoxicity and other metrics, such as size and ζ potential ($r^2 > 0.2$, SI Fig. S17).

Following successful replication of the synthesis by multiple operators, we established a scalable protocol that increased the reaction volume from 20 mL to 500 mL (SI Fig. S18), enabling synthesis at the multi-gram scale. The reactions were allowed to proceed overnight, nanoparticles were collected as described in the methods and the size and ζ potential was measured by DLS and ELS. We found no significant differences in the size, PDI or ζ potential of the resulting PAA@BSA@c-ZIF-8, PAA@CuBSA@c-ZIF-8 and PAA@FeBSA@c-ZIF-8 nanoparticles when compared to small batch sizes (Table S2).

Conclusion

Herein we demonstrate the iterative design of new H_2O_2 responsive PAA@CuBSA@c-ZIF-8 and PAA@FeBSA@c-ZIF-8 nanoparticles. We found that pre-association of BSA with Cu and Fe afforded the nanoparticles with Fenton-like chemistry, thereby enabling peroxide-responsive disassembly and controlled protein release. Through extensive characterization, including XPS, XRD, and DLS, we verified that the PAA@CuBSA@c-ZIF-8 and PAA@FeBSA@c-ZIF-8 nanoparticles retained their crystallinity, colloidal stability, and morphology when doped with transition metal ions. Moreover, we confirmed disassembly and release of protein and ions with the Bradford assay, DLS, and ICP-AES. IC_{50} values for HeLa cell cytotoxicity on a particle per mL basis while demonstrating the radical production and peroxide depletion mechanism with the DCF-DA assay and the peroxide concentration assay after particle incubation, respectively. Finally, we demonstrate that the synthesis presented here is highly reproducible across operators based on CQAs assessments and scalable synthesis, offering a route towards a translatable cancer treatment platform. We define DCF-DA response as an important CQA for PAA@CuBSA@c-ZIF-8 and PAA@FeBSA@c-ZIF-8 nanoparticle and defined its relevance for both current and future quality assurance metrics. In future iterations of this design, we suggest that inclusion of other therapeutic or targeting (bio) molecules would improve the cytotoxic and cytoselective effects of the nanoparticles. For example, active proteins such as glucose oxidase could be incorporated to enable starvation therapies, while targeting moieties like aptamers could facilitate cancer cell-specific delivery. As well, the tumour micro-environment is a highly complex matrix that contains varying levels of peroxide throughout its life cycle. As a result, it is unclear if the levels of hydrogen peroxide in real tumours would be sufficient to realize release and therapeutic potential. Future directions of this work should include the use of 3D cell culture models to assess if the release of protein and ions is both realistic and therapeutic at natural peroxide levels in tumours. Finally, the total released protein for PAA@CuBSA@c-ZIF-8 and PAA@FeBSA@c-ZIF-8 demonstrates
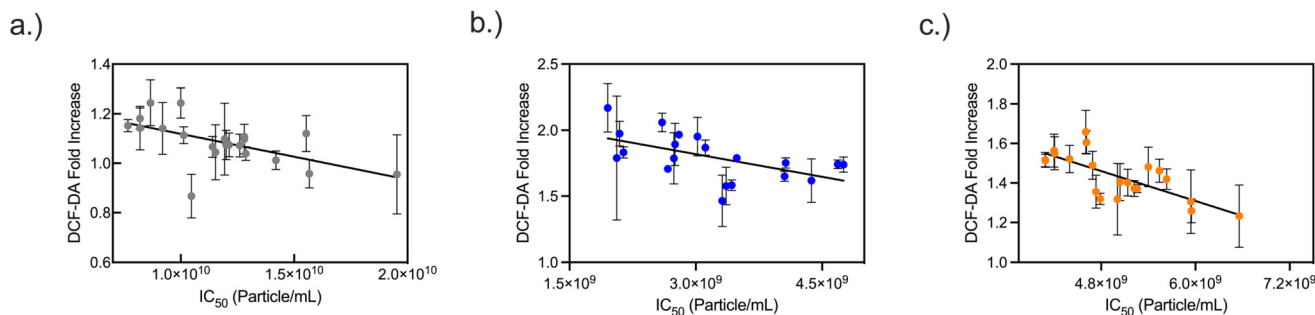
Fig. 8 The correlation between DCF-DA and IC_{50} of each nanoparticle investigated in this work. Each dot represents the average of three measurements, $n = 21$. (a) Shows the correlation for PAA@BSA@c-ZIF-8 ($r^2 = 0.3$) (b) shows the correlation for PAA@CuBSA@c-ZIF-8 ($r^2 = 0.4$) and (c) shows the correlation for PAA@FeBSA@c-ZIF-8 ($r^2 = 0.5$). Each point and error represent the average and standard deviation of three measurements from one batch, respectively.

proof of concept but is low and limits therapuetic relevance, therefore, future synthetic iterations will focus on tuning protein release for therapuetic action. This work provides a foundation for the development of highly reproducible, colloidally stable, stimuli-responsive ZIF-8-based nanomaterials towards a multimodal cancer therapy platform that integrates protein delivery, cation release, and ROS generation. We expect this platform to serve as a starting point for future researchers to investigate ROS-mediated release of therapeutics from nano-sized ZIF-8 constructs.

Author contributions

J. V. H. – conceptualization; methodology; formal analysis, investigation, data curation, writing – original draft, writing – review & editing, visualization, project administrationR. C. B. – methodology, investigation M. C. D. – validation, writing – review & editing K. E. – validation, writing – review & editing A. R. – validation, writing – review & editing, R. L. M. – investigation, methodology S. E. S. Q. – writing – review & editing, visualization, investigation, formal analysis, validation, methodology A. O. – resources, supervision, project administration, funding acquisition, writing – review & editing.

Conflicts of interest

There are no conflicts to declare.

Data availability

The data supporting this article have been included in the main text and supplementary information (SI) of this work. Supplementary information: standard operating procedures, iterative design data, reproducibility data, *etc*. See DOI: https://doi.org/10.1039/d5nr02870a.

Acknowledgements

References

1 B. Halliwell, M. V. Clement and L. H. Long, Hydrogen Peroxide in the Human Body, *FEBS Lett.*, 2000, 10–13, DOI: 10.1016/S0014-5793(00)02197-9.

2 D. Lee, S. Bae, Q. Ke, J. Lee, B. Song, S. A. Karumanchi, G. Khang, H. S. Choi and P. M. Kang, Hydrogen Peroxide-Responsive Copolyoxalate Nanoparticles for Detection and Therapy of Ischemia-Reperfusion Injury, *J. Controlled Release*, 2013, **172**, 1102–1110, DOI: 10.1016/j.jconrel.2013.09.020.

3 D. Trachootham, J. Alexandre and P. Huang, Targeting Cancer Cells by ROS-Mediated Mechanisms: A Radical Therapeutic Approach?, *Nat. Rev. Drug Discovery*, 2009, 579–591, DOI: 10.1038/nrd2803.

4 Z. Tang, P. Zhao, H. Wang, Y. Liu and W. Bu, Biomedicine Meets Fenton Chemistry, *Chem. Rev.*, 2021, **121**(4), 1981–2019, DOI: 10.1021/acs.chemrev.0c00977.

5 Y. Miao, X. Zhao, Y. Qiu, Z. Liu, W. Yang and X. Jia, Metal–Organic Framework-Assisted Nanoplatform with Hydrogen Peroxide/Glutathione Dual-Sensitive On-Demand Drug Release for Targeting Tumors and Their Microenvironment, *ACS Appl. Bio Mater.*, 2019, **2**(2), 895–905, DOI: 10.1021/acsabm.8b00741.

6 Y. Ma, R. Chen, X. Chen, Y. Sun, Y. Wang and B. Wang, A DNA-Engineered Metal-Organic-Framework Nanocarrier as a General Platform for Activatable Photodynamic Cancer Cell Ablation, *Nanoscale Adv.*, 2022, **5**(2), 361–367, DOI: 10.1039/d2na00509c.

7 D. Yu, M. Ma, Z. Liu, Z. Pi, X. Du, J. Ren and X. Qu, MOF-Encapsulated Nanozyme Enhanced SiRNA Combo: Control Neural Stem Cell Differentiation and Ameliorate Cognitive Impairments in Alzheimer's Disease Model, *Biomaterials*, 2020, **255**, 120160, DOI: 10.1016/j.biomaterials.2020.120160.

8 Z. Jin, P. Zhao, J. Zhang, T. Yang, G. Zhou, D. Zhang, T. Wang and Q. He, Intelligent Metal Carbonyl Metal–Organic Framework Nanocomplex for Fluorescent Traceable H_2O_2–Triggered CO Delivery, *Chem. – Eur. J.*, 2018, **24**(45), 11667–11674, DOI: 10.1002/chem.201801407.

9 H. Zheng, Y. Zhang, L. Liu, W. Wan, P. Guo, A. M. Nyström and X. Zou, One-Pot Synthesis of Metal–Organic Frameworks with Encapsulated Target Molecules and Their Applications for Controlled Drug Delivery, *J. Am. Chem. Soc.*, 2016, **138**(3), 962–968, DOI: 10.1021/jacs.5b11720.

10 J. Zhuang, C.-H. Kuo, L.-Y. Chou, D.-Y. Liu, E. Weerapana and C.-K. Tsung, Optimized Metal–Organic-Framework Nanospheres for Drug Delivery: Evaluation of Small-Molecule Encapsulation, *ACS Nano*, 2014, **8**(3), 2812–2819, DOI: 10.1021/nn406590q.

11 X. Chen, R. Tong, Z. Shi, B. Yang, H. Liu, S. Ding, X. Wang, Q. Lei, J. Wu and W. Fang, MOF Nanoparticles with Encapsulated Autophagy Inhibitor in Controlled Drug Delivery System for Antitumor, *ACS Appl. Mater. Interfaces*, 2018, **10**(3), 2328–2337, DOI: 10.1021/acsami.7b16522.

12 M. Gomar and S. Yeganegi, Adsorption of 5-Fluorouracil, Hydroxyurea and Mercaptopurine Drugs on Zeolitic Imidazolate Frameworks (ZIF-7, ZIF-8 and ZIF-9), *Microporous Mesoporous Mater.*, 2017, **252**, 167–172, DOI: 10.1016/j.micromeso.2017.06.010.

13 H. Kaur, G. C. Mohanta, V. Gupta, D. Kukkar and S. Tyagi, Synthesis and Characterization of ZIF-8 Nanoparticles for Controlled Release of 6-Mercaptopurine Drug, *J. Drug Delivery Sci. Technol.*, 2017, **41**, 106–112, DOI: 10.1016/j.jddst.2017.07.004.

14 T. Q. Pham, T. T. Nguyen, H. V. Nguyen, H. H. Do, T. H. Linh, H. T. T. Pham, L. H. T. Nguyen, M. T. Le and T. L. H. Doan, Nanoscale ZIF-8 as an Efficient Carboplatin Carrier for Targeted Cancer Therapy, *Inorg. Chem. Commun.*, 2024, **165**, 112567, DOI: 10.1016/j.inoche.2024.112567.

15 S. Kulkarni, A. Pandey, A. N. Nikam, S. H. Nannuri, S. D. George, S. M. A. Fayaz, A. P. Vincent and S. Mutalik, ZIF-8 Nano Confined Protein-Titanocene Complex Core-Shell MOFs for Efficient Therapy of Neuroblastoma: Optimization, Molecular Dynamics and Toxicity Studies, *Int. J. Biol. Macromol.*, 2021, **178**, 444–463, DOI: 10.1016/j.ijbiomac.2021.02.161.

16 J. Liu, Q. Wen, B. Zhou, C. Yuan, S. Du, L. Li, L. Jiang, S. Q. Yao and J. Ge, "Clickable" ZIF-8 for Cell-Type-Specific Delivery of Functional Proteins, *ACS Chem. Biol.*, 2022, **17**(1), 32–38, DOI: 10.1021/acschembio.1c00872.

17 L. Ding, X. Lin, Z. Lin, Y. Wu, X. Liu, J. Liu, M. Wu, X. Zhang and Y. Zeng, Cancer Cell-Targeted Photosensitizer and Therapeutic Protein Co-Delivery Nanoplatform Based on a Metal–Organic Framework for Enhanced Synergistic Photodynamic and Protein Therapy, *ACS Appl. Mater. Interfaces*, 2020, **12**(33), 36906–36916, DOI: 10.1021/acsami.0c09657.

18 S. Kumari, T. S. Howlett, R. N. Ehrman, S. Koirala, O. Trashi, I. Trashi, Y. H. Wijesundara and J. J. Gassensmith, *In Vivo* Biocompatibility of ZIF-8 for Slow Release *via* Intranasal Administration, *Chem. Sci.*, 2023, **14**(21), 5774–5782, DOI: 10.1039/D3SC00500C.

19 S. Kumari, Y. H. Wijesundara, T. S. Howlett, M. Waliullah, F. C. Herbert, A. Raja, I. Trashi, R. A. Bernal and J. J. Gassensmith, Biolistic Delivery of Liposomes Protected in Metal-Organic Frameworks, *Proc. Natl. Acad. Sci. U. S. A.*, 2023, **120**(11), e2218247120, DOI: 10.1073/pnas.2218247120.

20 A. F. Ogata, A. M. Rakowski, B. P. Carpenter, D. A. Fishman, J. G. Merham, P. J. Hurst and J. P. Patterson, Direct Observation of Amorphous Precursor Phases in the Nucleation of Protein–Metal–Organic Frameworks, *J. Am. Chem. Soc.*, 2020, **142**(3), 1433–1442, DOI: 10.1021/jacs.9b11371.

21 B. P. Carpenter, A. R. Talosig, J. T. Mulvey, J. G. Merham, J. Esquivel, B. Rose, A. F. Ogata, D. A. Fishman and J. P. Patterson, Role of Molecular Modification and Protein Folding in the Nucleation and Growth of Protein–Metal–Organic Frameworks, *Chem. Mater.*, 2022, **34**(18), 8336–8344, DOI: 10.1021/acs.chemmater.2c01903.

22 L. Schwartz, T. Seyfried, K. O. Alfarouk, J. D. Moreira and S. Fais, Out of Warburg Effect: An Effective Cancer Treatment Targeting the Tumor Specific Metabolism and Dysregulated PH, in *Seminars in Cancer Biology*, Academic Press, 2017, pp. 134–138. DOI: 10.1016/j.semcancer.2017.01.005.

23 L. Gaohua, X. Miao and L. Dou, Crosstalk of Physiological PH and Chemical PKa under the Umbrella of Physiologically Based Pharmacokinetic Modeling of Drug Absorption, Distribution, Metabolism, Excretion, and Toxicity, in *Expert Opinion on Drug Metabolism and Toxicology*, Taylor and Francis Ltd, 2021, pp. 1103–1124. DOI: 10.1080/17425255.2021.1951223.

24 L. E. Gerweck and K. Seetharaman, Cellular PH Gradient in Tumor versus Normal Tissue: Potential Exploitation for the Treatment of Cancer, *Cancer Res.*, 1996, **56**, 1194–1198.

25 H. Yang, S. Hu, H. Zhao, X. Luo, Y. Liu, C. Deng, Y. Yu, T. Hu, S. Shan, Y. Zhi, H. Su and L. Jiang, High-Performance Fe-Doped ZIF-8 Adsorbent for Capturing Tetracycline from Aqueous Solution, *J. Hazard. Mater.*, 2021, **416**, 126046, DOI: 10.1016/j.jhazmat.2021.126046.

26 M. T. Thanh, T. V. Thien, P. D. Du, N. P. Hung and D. Q. Khieu, Iron Doped Zeolitic Imidazolate Framework (Fe-ZIF-8): Synthesis and Photocatalytic Degradation of RDB Dye in Fe-ZIF-8, *J. Porous Mater.*, 2018, **25**, 857–869, DOI: 10.1007/s10934-017-0498-7.

27 Y. Zhong, Z. Peng, Y. Peng, B. Li, Y. Pan, Q. Ouyang, H. Sakiyama, M. Muddassir and J. Liu, Construction of Fe-Doped ZIF-8/DOX Nanocomposites for Ferroptosis Strategy in the Treatment of Breast Cancer, *J. Mater. Chem. B*, 2023, **11**, 6335–6345, DOI: 10.1039/d3tb00749a.

28 J. Liang, W. Zhang, J. Wang, W. Li, F. Ge, W. Jin and Y. Tao, Development of the Cu/ZIF-8 MOF Acid-Sensitive Nanocatalytic Platform Capable of Chemo/Chemodynamic Therapy with Improved Anti-Tumor Efficacy, *ACS Omega*, 2023, **8**, 19402–19412, DOI: 10.1021/acsomega.3c00269.

29 W. Gao, X. Han, L. Li, Y. Xu, M. Xu, Z. Gao and C. Wang, Functionalized ZIF-8 as a Versatile Platform for Drug Delivery and Cancer Therapy: Strategies, Challenges and Prospects, in *Journal of Materials Chemistry B*, Royal Society of Chemistry, 2025, DOI: 10.1039/d4tb02289k.

30 F. Wei, L. Hou, Y. Yao, Y. Lai, T. Lin, S. Zhao and D. Tang, An Intelligent Cu/ZIF-8-Based Nanodrug Delivery System for Tumor-Specific and Synergistic Therapy *via* Tumor Microenvironment-Responsive Cascade Reaction, *Microchim. Acta*, 2024, **191**(8), 447, DOI: 10.1007/s00604-024-06527-6.

31 N. Talukder, Y. Wang, B. B. Nunna, X. Tong and E. S. Lee, An Investigation on the Structural Stability of ZIF-8 in Water versus Water-Derived Oxidative Species in Aqueous Environment, *Microporous Mesoporous Mater.*, 2024, **366**, 112938, DOI: 10.1016/j.micromeso.2023.112934.

32 A. N. Pham, G. Xing, C. J. Miller and T. D. Waite, Fenton-like Copper Redox Chemistry Revisited: Hydrogen Peroxide and Superoxide Mediation of Copper-Catalyzed Oxidant Production, *J. Catal.*, 2013, **301**, 54–64, DOI: 10.1016/j.jcat.2013.01.025.

33 S. Li, L. Liang, L. Tian, J. Wu, Y. Zhu, Y. Qin, S. Zhao and F. Ye, Enhanced Peroxidase-like Activity of MOF Nanozymes by Co-Catalysis for Colorimetric Detection of Cholesterol, *J. Mater. Chem. B*, 2023, **11**, 7913, DOI: 10.1039/D3TB00958K.

34 J. Van Houten, R. C. Barberi, J. King and A. F. Ogata, Improving the Colloidal Stability of Protein@ZIF-8 Nanoparticles in Biologically Relevant Buffers, *Mater. Adv.*, 2024, **5**(14), 5945–5957, DOI: 10.1039/D4MA00377B.

35 J. Van Houten, A. Dosajh, S. Gulati, G. Bhullar, C. Copeman and A. F. Ogata, Morphology Control of Self-Assembled Copper Coordination Polymers for Glucose Assays, *Langmuir*, 2024, **40**(7), 3486–3495, DOI: 10.1021/acs.langmuir.3c02979.

36 V. Sharma, D. Anderson and A. Dhawan, Zinc Oxide Nanoparticles Induce Oxidative DNA Damage and ROS-Triggered Mitochondria Mediated Apoptosis in Human Liver Cells (HepG2), *Apoptosis*, 2012, **17**, 852–870, DOI: 10.1007/s10495-012-0705-6.

37 D. A. Gómez-Gualdrón, P. Z. Moghadam, J. T. Hupp, O. K. Farha and R. Q. Snurr, Application of Consistency Criteria To Calculate BET Areas of Micro- And Mesoporous Metal–Organic Frameworks, *J. Am. Chem. Soc.*, 2016, **138**(1), 215–224, DOI: 10.1021/jacs.5b10266.

38 A. Belatik, S. Hotchandani, R. Carpentier and H. A. Tajmir-Riahi, Locating the Binding Sites of Pb(II) Ion with Human and Bovine Serum Albumins, *PLoS One*, 2012, 7(5), e36723, DOI: 10.1371/journal.pone.0036723.

39 W. Bal, M. Sokołowska, E. Kurowska and P. Faller, Binding of Transition Metal Ions to Albumin: Sites, Affinities and Rates, *Biochim. Biophys. Acta, Gen. Subj.*, 2013, 5444–5455, DOI: 10.1016/j.bbagen.2013.06.018.

40 M. T. Behnamfar, H. Hadadzadeh, J. Simpson, F. Darabi, A. Shahpiri, T. Khayamian, M. Ebrahimi, H. A. Rudbari and M. Salimi, Experimental and Molecular Modeling Studies of the Interaction of the Polypyridyl Fe(II) and Fe(III) Complexes with DNA and BSA, *Spectrochim. Acta, Part A*, 2015, **134**, 502–516, DOI: 10.1016/j.saa.2014.06.105.

41 X. Xu, L. Zhang, D. Shen, H. Wu and Q. Liu, Oxygen-Dependent Oxidation of Fe(II) to Fe(III) and Interaction of Fe(III) with Bovine Serum Albumin, Leading to a Hysteretic Effect on the Fluorescence of Bovine Serum Albumin, *J. Fluoresc.*, 2008, **18**, 193–201, DOI: 10.1007/s10895-007-0263-4.

42 R. A. Bradshaw, W. T. Shearer and F. R. Gurd, Sites of Binding of Copper(II) Ion by Peptide (1–24) of Bovine Serum Albumin, *J. Biol. Chem.*, 1968, **243**, 3817–3825, DOI: 10.1016/s0021-9258(18)92017-x.

43 Y. Zhang and D. E. Wilcox, Thermodynamic and Spectroscopic Study of Cu(II) and Ni(II) Binding to Bovine Serum Albumin, *J. Biol. Inorg. Chem.*, 2002, **7**, 327–337, DOI: 10.1007/s00775-001-0302-6.

44 T. Peters and F. A. Blumenstock, Copper-Binding Properties of Bovine Serum Albumin and Its Amino-Terminal Peptide Fragment, *J. Biol. Chem.*, 1967, **242**, 1574–1578, DOI: 10.1016/s0021-9258(18)96130-2.

45 N. Schwierz, D. Horinek and R. R. Netz, Anionic and Cationic Hofmeister Effects on Hydrophobic and Hydrophilic Surfaces, *Langmuir*, 2013, **29**(8), 2602–2614, DOI: 10.1021/la303924e.

46 R. I. Slavchov, B. Peychev and I. Minkov, Electrolytes at Uncharged Liquid Interfaces: Adsorption, Potentials, Surface Tension, and the Role of the Surfactant Monolayer, *Langmuir*, American Chemical Society, 2024. DOI: 10.1021/acs.langmuir.4c01388.

47 A. Kumar, D. Maity, G. Vyas, M. Bhatt, S. Bhatt and P. Paul, Polyacrylic Acid@zeolitic Imidazolate Framework-8 Nanoparticles for Detection and Absorptive Removal of Cyanide from Aqueous Media with High Efficiency, *Colloids Surf., A*, 2021, **617**, 126358, DOI: 10.1016/j.colsurfa.2021.126358.

48 S. Yamane, A. H. B. Yusri, P. y. Chen, A. J. van der Vlies, A. B. Mabrouk, I. Fetzer and U. Hasegawa, Surface Coating of ZIF-8 Nanoparticles with Polyacrylic Acid: A Facile Approach to Enhance Chemical Stability for Biomedical Applications, *Macromol. Biosci.*, 2024, **25**(2), 2400382, DOI: 10.1002/mabi.202400382.

49 T. Li, W. Zhang, S. Zhai, G. Gao, J. Ding, W. Zhang, Y. Liu, X. Zhao, B. Pan and L. Lv, Efficient Removal of Nickel(II) from High Salinity Wastewater by a Novel PAA/ZIF-8/PVDF Hybrid Ultrafiltration Membrane, *Water Res.*, 2018, **143**, 87–98, DOI: 10.1016/j.watres.2018.06.031.

50 F. Tian, A. M. Cerro, A. M. Mosier, H. K. Wayment-Steele, R. S. Shine, A. Park, E. R. Webster, L. E. Johnson, M. S. Johal and L. Benz, Surface and Stability Characterization of a Nanoporous ZIF-8 Thin Film, *J. Phys. Chem. C*, 2014, **118**(26), 14449–14456, DOI: 10.1021/jp5041053.

51 H. Wang, H. You, G. Wu, L. Huang, J. Yan, X. Liu, Y. Ma, M. Wu, Y. Zeng, J. Yu and H. Zhang, Co/Fe Co-Doped ZIF-8 Derived Hierarchically Porous Composites as High-Performance Electrode Materials for Cu2+ Ions Capacitive Deionization, *Chem. Eng. J.*, 2023, **460**, 141621, DOI: 10.1016/j.cej.2023.141621.

52 S. Sun, Z. Yang, J. Cao, Y. Wang and W. Xiong, Copper-Doped ZIF-8 with High Adsorption Performance for Removal of Tetracycline from Aqueous Solution, *J. Solid State Chem.*, 2020, **285**, 121219, DOI: 10.1016/j.jssc.2020.121219.

53 K. Liang, R. Ricco, C. M. Doherty, M. J. Styles, S. Bell, N. Kirby, S. Mudie, D. Haylock, A. J. Hill, C. J. Doonan and P. Falcaro, Biomimetic Mineralization of Metal-Organic

Frameworks as Protective Coatings for Biomacromolecules, *Nat. Commun.*, 2015, **6**(1), 7240, DOI: 10.1038/ncomms8240.

54 V. Filipe, A. Hawe and W. Jiskoot, Critical Evaluation of Nanoparticle Tracking Analysis (NTA) by NanoSight for the Measurement of Nanoparticles and Protein Aggregates, *Pharm. Res.*, 2010, **27**, 796–810, DOI: 10.1007/s11095-010-0073-2.

55 J. Gao, W. Chu, X. Ding, L. Ding, Q. Guo and Y. Fu, Degradation Kinetic Studies of BSA@ZIF-8 Nanoparticles with Various Zinc Precursors, Metal-to-Ligand Ratios, and PH Conditions, *ACS Omega*, 2023, **8**(47), 44601–44610, DOI: 10.1021/acsomega.3c04973.

56 T.-T. Chen, J.-T. Yi, Y.-Y. Zhao and X. Chu, Biomineralized Metal–Organic Framework Nanoparticles Enable Intracellular Delivery and Endo-Lysosomal Release of Native Active Proteins, *J. Am. Chem. Soc.*, 2018, **140**(31), 9912–9920, DOI: 10.1021/jacs.8b04457.

57 M. Joharian, A. Uzel, A. Elloumi, Y. Nedellec, T. Encinas, S. Gambarelli and A. J. Gross, Redox-Active Biomineralised Zeolitic Imidazolate Frameworks Enable Peroxidase Bioelectrocatalysis with Shielding against Substrate Inhibition and Thermal Inactivation, *J. Mater. Chem. A*, 2025, **13**(37), 31699–31713, DOI: 10.1039/D5TA02717A.

58 Z. Németh, I. Csóka, R. S. Jazani, B. Sipos, H. Haspel, G. Kozma, Z. Kónya and D. G. Dobó, Quality by Design-Driven Zeta Potential Optimisation Study of Liposomes with Charge Imparting Membrane Additives, *Pharmaceutics*, 2022, **14**(9), 1798, DOI: 10.3390/pharmaceutics14091798.

59 B. W. Ninham, On Progress in Forces since the DLVO Theory, in *Advances in Colloid and Interface Science*, Elsevier Science Publishers B.V, 1999, pp. 1–17. DOI: 10.1016/S0001-8686(99)00008-1.

60 X. Yang, Q. Tang, Y. Jiang, M. Zhang, M. Wang and L. Mao, Nanoscale ATP-Responsive Zeolitic Imidazole Framework-90 as a General Platform for Cytosolic Protein Delivery and Genome Editing, *J. Am. Chem. Soc.*, 2019, **141**(9), 3782–3786, DOI: 10.1021/jacs.8b11996.

61 X. Xu, C. Liu, S. Wang, E. Mäkilä, J. Wang, O. Koivisto, J. Zhou, J. M. Rosenholm, Y. Shu and H. Zhang, Microfluidic-Assisted Biomineralization of CRISPR/Cas9 in near-Infrared Responsive Metal–Organic Frameworks for Programmable Gene-Editing, *Nanoscale*, 2022, **14**(42), 15832–15844, DOI: 10.1039/D2NR04095F.

62 Y. Jiang, X. Pan, M. Yao, L. Han, X. Zhang, Z. Jia, J. Weng, W. Chen, L. Fang, X. Wang, Y. Zhang, R. Duan, F. Ren, K. Wang, X. Chen and X. Lu, Bioinspired Adhesive and Tumor Microenvironment Responsive NanoMOFs Assembled 3D-Printed Scaffold for Anti-Tumor Therapy and Bone Regeneration, *Nano Today*, 2021, **39**, 101182, DOI: 10.1016/j.nantod.2021.101182.

63 D. P. Barondeau and E. D. Getzoff, Structural Insights into Protein–Metal Ion Partnerships, *Curr. Opin. Struct. Biol.*, 2004, **14**(6), 765–774, DOI: 10.1016/j.sbi.2004.10.012.

64 W. W. H. Law, V. Kanelis and D. B. Zamble, Biochemical Studies Highlight Determinants for Metal Selectivity in the *Escherichia Coli* Periplasmic Solute Binding Protein NikA, *Metallomics*, 2022, (11), 14, DOI: 10.1093/mtomcs/mfac084.

65 E. Asante-Appiah and A. M. Skalka, A Metal-Induced Conformational Change and Activation of HIV-1 Integrase, *J. Biol. Chem.*, 1997, **272**(26), 16196–16205.

66 A. Bujacz, Structures of Bovine, Equine and Leporine Serum Albumin, *Acta Crystallogr., Sect. D: Biol. Crystallogr.*, 2012, **68**(10), 1278–1289, DOI: 10.1107/S0907444912027047.

67 R. Lu, W.-W. Li, A. Katzir, Y. Raichlin, H.-Q. Yu and B. Mizaikoff, Probing the Secondary Structure of Bovine Serum Albumin during Heat-Induced Denaturation Using Mid-Infrared Fiberoptic Sensors, *Analyst*, 2015, **140**(3), 765–770, DOI: 10.1039/C4AN01495B.

68 R. G. Reed, R. C. Feldhoff, O. L. Clute and T. Peters, Fragments of Bovine Serum Albumin Produced by Limited Proteolysis. Conformation and Ligand Binding, *Biochemistry*, 1975, **14**(21), 4578–4583, DOI: 10.1021/bi00692a004.

69 A. Lesniak, A. Campbell, M. P. Monopoli, I. Lynch, A. Salvati and K. A. Dawson, Serum Heat Inactivation Affects Protein Corona Composition and Nanoparticle Uptake, *Biomaterials*, 2010, **31**(36), 9511–9518, DOI: 10.1016/j.biomaterials.2010.09.049.

70 K. Malhotra, B. Kumar, P. A. E. Piunno and U. J. Krull, Cellular Uptake of Upconversion Nanoparticles Based on Surface Polymer Coatings and Protein Corona, *ACS Appl. Mater. Interfaces*, 2024, **16**(28), 35985–36001, DOI: 10.1021/acsami.4c04148.

71 S. Behzadi, V. Serpooshan, R. Sakhtianchi, B. Müller, K. Landfester, D. Crespy and M. Mahmoudi, Protein Corona Change the Drug Release Profile of Nanocarriers: The "Overlooked" Factor at the Nanobio Interface, *Colloids Surf., B*, 2014, **123**, 143–149, DOI: 10.1016/j.colsurfb.2014.09.009.

72 S. McColman, R. Li, S. Osman, A. Bishop, K. P. Wilkie and D. T. Cramb, Serum Proteins on Nanoparticles: Early Stages of the "Protein Corona", *Nanoscale*, 2021, **13**(48), 20550–20563, DOI: 10.1039/D1NR06137B.

73 P. Tsvetkov, S. Coy, B. Petrova, M. Dreishpoon, A. Verma, M. Abdusamad, J. Rossen, L. Joesch-Cohen, R. Humeidi, R. D. Spangler, J. K. Eaton, E. Frenkel, M. Kocak, S. M. Corsello, S. Lutsenko, N. Kanarek, S. Santagata and T. R. Golub, Copper Induces Cell Death by Targeting Lipoylated TCA Cycle Proteins, *Science*, 2022, **375**, 1254–1261, DOI: 10.1126/science.abf0529.

74 S. J. Dixon, K. M. Lemberg, M. R. Lamprecht, R. Skouta, E. M. Zaitsev, C. E. Gleason, D. N. Patel, A. J. Bauer, A. M. Cantley, W. S. Yang, B. Morrison and B. R. Stockwell, Ferroptosis: An Iron-Dependent Form of Nonapoptotic Cell Death, *Cell*, 2012, **149**, 1060–1072, DOI: 10.1016/j.cell.2012.03.042.

75 W. Maret, Molecular Aspects of Human Cellular Zinc Homeostasis: Redox Control of Zinc Potentials and Zinc Signals, *BioMetals*, 2009, **22**, 149–157, DOI: 10.1007/s10534-008-9186-z.

76   L. J. Jiang, W. Maret and B. L. Vallee, The ATP-Metallothionein Complex, *Proc. Natl. Acad. Sci. U. S. A.*, 1998, **95**, 9146–9149, DOI: 10.1073/pnas.95.16.9146.

77   T. L. Riss, R. A. Moravec, A. L. Niles, S. Duellman, H. A. Benink, T. J. Worzella and L. Minor, *Cell Viability Assays*, 2013.

78   Y. Wu, T. Guo, Y. Qiu, Y. Lin, Y. Yao, W. Lian, L. Lin, J. Song and H. Yang, An Inorganic Prodrug, Tellurium Nanowires with Enhanced ROS Generation and GSH Depletion for Selective Cancer Therapy, *Chem. Sci.*, 2019, **10**, 7068–7075, DOI: 10.1039/c9sc01070j.

79   R. Han, K. S. Walton and D. S. Sholl, Does Chemical Engineering Research Have a Reproducibility Problem?, *Annu. Rev. Chem. Biomol. Eng.*, 2019, **10**(1), 43–57, DOI: 10.1146/annurev-chembioeng-060718-030323.

80   H. S. Leong, K. S. Butler, C. J. Brinker, M. Azzawi, S. Conlan, C. Dufés, A. Owen, S. Rannard, C. Scott, C. Chen, M. A. Dobrovolskaia, S. V. Kozlov, A. Prina-Mello, R. Schmid, P. Wick, F. Caputo, P. Boisseau, R. M. Crist, S. E. McNeil, B. Fadeel, L. Tran, S. F. Hansen, N. B. Hartmann, L. P. W. Clausen, L. M. Skjolding, A. Baun, M. Ågerstrand, Z. Gu, D. A. Lamprou, C. Hoskins, L. Huang, W. Song, H. Cao, X. Liu, K. D. Jandt, W. Jiang, B. Y. S. Kim, K. E. Wheeler, A. J. Chetwynd, I. Lynch, S. M. Moghimi, A. Nel, T. Xia, P. S. Weiss, B. Sarmento, J. das Neves, H. A. Santos, L. Santos, S. Mitragotri, S. Little, D. Peer, M. M. Amiji, M. J. Alonso, A. Petri-Fink, S. Balog, A. Lee, B. Drasler, B. Rothen-Rutishauser, S. Wilhelm, H. Acar, R. G. Harrison, C. Mao, P. Mukherjee, R. Ramesh, L. R. McNally, S. Busatto, J. Wolfram, P. Bergese, M. Ferrari, R. H. Fang, L. Zhang, J. Zheng, C. Peng, B. Du, M. Yu, D. M. Charron, G. Zheng and C. Pastore, On the Issue of Transparency and Reproducibility in Nanomedicine, in *Nature Nanotechnology*, Nature Publishing Group, 2019, pp. 629–635. DOI: 10.1038/s41565-019-0496-9.

81   M. Faria, M. Björnmalm, K. J. Thurecht, S. J. Kent, R. G. Parton, M. Kavallaris, A. P. R. Johnston, J. J. Gooding, S. R. Corrie, B. J. Boyd, P. Thordarson, A. K. Whittaker, M. M. Stevens, C. A. Prestidge, C. J. H. Porter, W. J. Parak, T. P. Davis, E. J. Crampin and F. Caruso, Minimum Information Reporting in Bio–Nano Experimental Literature, *Nat. Nanotechnol.*, 2018, **13**, 777–785, DOI: 10.1038/s41565-018-0246-4.

82   C. M. Dawidczyk, L. M. Russell and P. C. Searson, Recommendations for Benchmarking Preclinical Studies of Nanomedicines, in *Cancer Research*, American Association for Cancer Research Inc, 2015, pp. 4016–4020. DOI: 10.1158/0008-5472.CAN-15-1558.

83   A. Tropsha, K. C. Mills and A. J. Hickey, Reproducibility, Sharing and Progress in Nanomaterial Databases, in *Nature Nanotechnology*, Nature Publishing Group, 2017, pp. 1111–1114. DOI: 10.1038/nnano.2017.233.

84   Health Canada, *Guidance Document – Pharmaceutical Development – ICH Topic Q8(R2)*, 2016.

85   U.S. Department of Health and Human Services, Food and Drug Administration; Center for Drug Evaluation and Research; Center for Biologics Evaluation and Research, in *Guidance for Industry Q8(R2) Pharmaceutical Development*; 2009.

86   U.S. Department of Health and Human Services, Food and Drug Administration; Center for Drug Evaluation and Research; Center for Biologics Evaluation and Research, in *Drug Products, Including Biological Products, That Contain Nanomaterials - Guidance for Industry*, 2022.

87   M. Xu, Y. Qi, G. Liu, Y. Song, X. Jiang and B. Du, Size-Dependent *In Vivo* Transport of Nanoparticles: Implications for Delivery, Targeting, and Clearance, *ACS Nano*, 2023, **17**(21), 20825–20849, DOI: 10.1021/acsnano.3c05853.

88   C. He, Y. Hu, L. Yin, C. Tang and C. Yin, Effects of Particle Size and Surface Charge on Cellular Uptake and Biodistribution of Polymeric Nanoparticles, *Biomaterials*, 2010, **31**, 3657–3666, DOI: 10.1016/j.biomaterials.2010.01.065.

89   Y. Zhang, M. Yang, N. G. Portney, D. Cui, G. Budak, E. Ozbay, M. Ozkan and C. S. Ozkan, Zeta Potential: A Surface Electrical Characteristic to Probe the Interaction of Nanoparticles with Normal and Cancer Human Breast Epithelial Cells, *Biomed. Microdevices*, 2008, **10**, 321–328, DOI: 10.1007/s10544-007-9139-2.

90   S. Patil, A. Sandberg, E. Heckert, W. Self and S. Seal, Protein Adsorption and Cellular Uptake of Cerium Oxide Nanoparticles as a Function of Zeta Potential, *Biomaterials*, 2007, **28**, 4600–4607, DOI: 10.1016/j.biomaterials.2007.07.029.

91   M. T. Manzari, Y. Shamay, H. Kiguchi, N. Rosen, M. Scaltriti and D. A. Heller, Targeted Drug Delivery Strategies for Precision Medicines, in *Nature Reviews Materials*, Nature Research, 2021, pp. 351–370. DOI: 10.1038/s41578-020-00269-6.